

Multi-purpose InSTRument for Astronomy at Low-resolution: MISTRAL@OHP [★]

J. Schmitt¹, C. Adami², M. Dennefeld³,
F. Agneray², S. Basa^{1,2}, J.C. Brunel¹, V. Buat², D. Burgarella², C. Carvalho³, G. Castagnoli¹, N. Grosso², F. Huppert¹,
C. Moreau², F. Moreau¹, L. Moreau¹, E. Muslimov², S. Pascal¹, S. Perruchot¹, D. Russeil²,
J.L. Beuzit⁴, F. Dolon¹, M. Ferrari^{1,2}, B. Hamelin⁴, A. LevanSuu¹,
K. Aravind⁵, D. Gotz⁷, E. Jehin⁶, E. LeFloc'h⁷, J. Palmerio⁸, A. Saccardi⁸, B. Schneider^{7,9}, F. Schüssler¹⁰, D. Turpin⁷,
and S.D. Vergani⁸

¹ OHP, OSU - Institut Pythéas, UAR 3470, CNRS, Aix-Marseille Université, 1912 Route de l'Observatoire, 04870 St.Michel l'Observatoire, France

² Aix Marseille Univ, CNRS, CNES, LAM, Marseille, France

³ Sorbonne Université, CNRS, UMR 7095, Institut d'Astrophysique de Paris, 98bis Bd Arago, 75014 Paris, France

⁴ OSU - Institut Pythéas, UAR 3470, CNRS, Aix-Marseille Université, Pôle de l'Étoile Site de Château-Gombert 38, rue Frédéric Joliot-Curie 13388 Marseille, France

⁵ Physical Research Laboratory, Navarangpura, Ahmedabad, 380058, Gujarat, India

⁶ Space sciences, Technologies & Astrophysics Research (STAR) Institute, Allée du Six Août, 19C, University of Liège, 4000 Liège, Belgium

⁷ CEA, IRFU, DAp, AIM, Université Paris-Saclay, Université Paris Cité, Sorbonne Paris Cité, CNRS, F-91191 Gif-sur-Yvette, France

⁸ GEPI, Observatoire de Paris, Université PSL, CNRS, 5 Place Jules Janssen, 92190 Meudon, France

⁹ Kavli Institute for Astrophysics and Space Research, Massachusetts Institute of Technology, Cambridge, MA, USA

¹⁰ IRFU, CEA, Université Paris-Saclay, Gif-sur-Yvette, France

Accepted . Received ; Draft printed: April 8, 2024

ABSTRACT

Context. MISTRAL is the new Faint Object Spectroscopic Camera mounted at the folded Cassegrain focus of the 1.93m telescope of Haute-Provence Observatory.

Aims. We describe the design and components of the instrument and give some details about its operation.

Methods. We emphasise in particular the various observing modes and the performances of the detector. A short description is also given about the working environment. Various types of objects, including stars, nebulae, comets, novae, galaxies have been observed during various test phases to evaluate the performances of the instrument.

Results. The instrument covers the range of 4000 to 8000 Å with the blue setting, or from 6000 to 10000 Å with the red setting, at an average spectral resolution of 700. Its peak efficiency is about 22% at 6000 Å. In spectroscopy, a limiting magnitude of $r \sim 19.5$ can be achieved for a point source in one hour with a signal to noise of 3 in the continuum (and better if emission lines are present). In imaging mode, limiting magnitudes of 20-21 can be obtained in 10-20mn (with average seeing conditions of 2.5 arcsec at OHP). The instrument is very users-friendly and can be put into operations in less than 15mn (rapid change-over from the other instrument in use) if required by the science (like for Gamma-Rays Bursts). Some first scientific results are described for various types of objects, and in particular for the follow-up of GRBs.

Conclusions. While some further improvements are still under way, in particular to ease the switch from blue to red setting and add more grisms or filters, MISTRAL is ready for the follow-up of transients and other variable objects, in the soon-to-come era of e.g. the SVOM satellite and of the Rubin telescope.

Key words. Haute-Provence Observatory, Spectrographs, Optical components, Transient Sky.

1. Introduction

Since the early 2010th, with the advent of many new sky surveys, both from the ground and from space, the exploration of the variable sky is becoming a highly competitive new domain of Astrophysics (e.g. Graham et al. (2019), and references

therein). The high cadence of those surveys in the framework of Multi-messenger astrophysics, and the large area covered by them leads to the discovery of a wealth of new phenomena and classes of objects, enlarging the observed physical diversity, as well as improving the statistics on previously known types of objects. This will still increase in the near future, with the advent of the Rubin Telescope (former LSST) and the launch of SVOM, thus requiring a major effort of ground-based follow-up. On the high-energy side, Gamma-Rays bursts (GRBs, e.g. Gehrels et al. (2009)) are observed in large numbers, and clas-

Send offprint requests to: C. Adami e-mail: christophe.adami@lam.fr

* Based on observations obtained with Observatoire de Haute-Provence (OHP) instruments (see acknowledgements for more details).

sified into two categories, the short- and long-duration GRBs. On the Supernovae (SNe) side (e.g. Gal-Yam (2017)), it appears that the early classification in types I or II explosions needs to be refined, to take into account the variety of observed phenomena: not just core-collapse, or thermonuclear explosions of CO white dwarfs, but including now ultraluminous SNe or faint and fast decaying type I SNe, He detonations Ia objects or objects interacting with the circum-stellar medium (CSM), not forgetting the variety of novae. The range of underlying physical mechanisms is therefore much more diverse than previously thought, but is still not understood. On a somewhat quieter side, Luminous Blue Variables, or the numerous peculiar binaries await a better understanding too.

Non transient, but variable objects also require some follow-up. For instance, it has been recently found that some quasars are showing dramatic changes in luminosity and spectral characteristics, the so-called Changing Look Quasars (e.g. MacLeod et al. (2016) and references therein), whose changes are not compatible with the Standard Active Galactic Nuclei (AGN) model: more and more objects are found of that kind, and they require more long-term monitoring, to measure timescales and possible delays between the changes in the optical and in other wavelengths.

On the other hand, large spectroscopic catalogs (e.g. SDSS¹) are rarely 100% complete or are not always covering the high latitude regions (see e.g. the XCLASS survey, Koulouridis et al. (2021)). Moreover, spectra available in the literature are sometimes of poor quality, as they were just made to get a redshift or a general classification of the objects, with insufficient signal-to-noise ratio to detect faint characteristic lines, or too short a spectral coverage to e.g. explore the red part of the spectrum. What is most needed to progress in all these fields is enough ground-based observing time to follow over time the evolution of representative examples of all those categories. Both photometry, and, even more, spectroscopy is required, including, if possible, the near infrared: only with long time series of data is it possible to understand the underlying physical mechanisms. Small to medium sized telescopes are now more available for long time series than the 8m ones, and are well suited, provided they are equipped with efficient versatile spectro-imagers. Observatoire de Haute Provence (OHP) had been pioneer in the early exploration of the far-red range (6000-11000 Å), first with the Roucass spectrograph (Andrillat et al. (1975)), and later with the Carelec spectrograph (Lemaitre et al. (1990)), but since the decommissioning of the latter in 2012, no low dispersion spectroscopic facility was available anymore, at a moment where it is much needed again.

It is with this in mind that the MISTRAL² (Multi-purpose InSTRument for Astronomy at Low-dispersion) instrument had been planned for the OHP 1.93m telescope, with a possibility of rapid reaction (Targets of Opportunity) and changeover from the other OHP T193 instrument, SOPHIE. While the concept of the focal reducer was invented by G. Courtes in Marseille (Courtès (1960)) long ago, no such instrument was permanently installed at OHP. With the development of Transient Astronomy, such a flexible instrument became mandatory and was envisaged already for the launch of Gaia Alerts. Various issues delayed the project (see below), but the gap is now filled in, and the MISTRAL instrument entered into service in 2021.

MISTRAL can be operated in two modes: regular observing runs in visitor mode and Target of Opportunity (ToO) mode with service observing for fast transients. MISTRAL can be accessed by any astronomer working in a french astronomical institution via the national call for observing proposals, which uses the NorthStar³ system. Non-nationals can also access it through the Transnational Access Program of the Opticon RadioNet Pilot program⁴, which includes a wide range of worldwide institutions⁵.

In the next section, we describe the MISTRAL main components, give some details on the operation mode and tools available for the observer. As on-sky instrument performance validations, we present in section 3 real observations demonstrating MISTRAL's ability to access faint objects of various types, including access to near infrared lines (such as the Paschen lines), and to spectroscopically classify them. To assess MISTRAL's ability to obtain higher spectral resolution spectra, we also investigate MISTRAL's spectral resolution around H α . This section finally shows that we can follow moving targets with a report of a comet follow-up. Section 4 reports about the core of MISTRAL's activities: GRB follow-ups. We detail in this section several observations with an intrinsic scientific interest (e.g. the "BOAT"). Finally, more details about the instrument operations are given in the annexes.

2. General instrument description

2.1. General set-up

A versatile spectro-imager should cover as large a wavelength range as possible, to cover the various science goals described above. But this wish is limited by the size of the detector, here a single one with 2048 pixels. While the initial idea was then to follow the path of SPRAT at the Liverpool telescope (Pascik (2017)), to speed up the development, it rapidly became clear that several factors were preventing this simple approach. First of all, the 1.93m telescope being a relatively old telescope, its f/ratio at Cassegrain focus is f/15, contrary to more modern telescopes which are at f/10 or faster: to avoid too long an instrument, a focal reducer had thus to be introduced. Second, since the decommissioning of the Carelec, the main instrument at the 1.93m was a high-resolution spectrograph for exoplanets research with the velocimetry technique (SOPHIE), requiring a good long-term stability. Rapid change-overs needed for ToO observations were therefore not compatible with this requirement. Of course, the ideal solution would have been a common adapter for both instruments (SOPHIE being anyway fed by fibers) but this could not be implemented in time. It was therefore decided to mount MISTRAL at the folded Cassegrain focus, the change-over from one to the other instrument being done simply by putting/removing a flat 45° mirror in the main beam: the change-over is done this way in less than 15 minutes (including adjustment of the telescope focus). While having then anyway to change the mechanical design with respect to SPRAT, we took advantage of those changes to implement more flexibility in the instrument, like introducing a filter holder and a grism holder, where different components can be introduced in the parallel beam by simply moving (sliding) those holders: the exchange is done in a few seconds. The large OHP telescopes being operated with a Telescope Operator on site, this relaxed a bit the

¹ <https://skyserver.sdss.org/dr18>

² http://www.obs-hp.fr/guide/mistral/MISTRAL_spectrograph_camera.shtml

³ <https://northstar.omp.eu/>

⁴ <https://www.orp-h2020.eu/>

⁵ <https://www.orp-h2020.eu/partner>

constraints on mechanical and pointing accuracy, as the acquisition and centering into the slit is always checked visually.

Regarding the mechanical design, within the T193 Cassegrain Adapter, there is a motorised 45° flat mirror which needs to be moved in the beam to redirect the light onto MISTRAL (at the folded Cassegrain focus) or moved out of the beam for the other instrument, SOPHIE, which is fed at the direct Cassegrain focus. MISTRAL is mounted on one of the side slots of the T193 Adapter, the other one, opposite, being still empty. Fig.1 shows the instrument. The focusing on the slit is done by moving the secondary mirror of the telescope, while the focusing on the detector is done by moving the detector holder. A guiding camera is associated directly to the instrument to minimise mechanical flexures⁶.



Fig. 1. MISTRAL (to the left of the image) installed at the folded Cassegrain focus of the 1.93m telescope at OHP

These modifications lead nevertheless to a relatively simple instrument, with a long term stability (see Appendix F) as it is permanently mounted to the telescope and very easy to operate for first time users.

2.2. Optical Path and Detector

MISTRAL is mounted at the folded-Cassegrain focus of the 1.93m telescope via a focal reducer. This focal reducer reduces the beam from F/15 to F/6 at the entrance slit. At the exit on the detector, the opening is F/3. The entrance slit is presently fixed at a 112 microns width, translating into 1.9'' on the sky, but a variable slit is under construction (the average seeing at OHP is around 2''). At the end, the beam falls on an ANDOR deep depletion 2K×2K CCD camera (iKon-L DZ936N BEX2DD CCD-22031) with 13.5 μ pixels, giving therefore slightly more than 4 pixels per slit width on the detector. This allows for some smoothing in the spectra to increase the signal to noise ratio if needed. The cooling is made by a 5-layer Peltier device. The operating temperature is -90C to -95C. The dark current is lower than 3 electrons/hour/pixel. The sliding plate holding the gratings has presently two gratings, for the blue (roughly 4000-8000 Å) or the red (6000-10000 Å) range, but two more slots are available. The spectral resolution is about 700 at 6000 Å (see Appendix C for more details). The FLI filter wheel has 12 positions for 50 mm filters (available presently are : SDSS g', r', i', z' + Y, OIII, Hα, SII, see also appendix B). Four Thorlabs motors are used to move/remove elements in/out of the optical

⁶ http://www.obs-hp.fr/guide/mistral/MISTRAL_spectrograph_camera.shtml#H5

path: the slit, the gratings, the filters and the calibration mirror. Calibration lights (Hg Ar Xe spectral lamps and a Tungsten flat-field lamp) are inserted within the optical path by four optical fibers via the calibration mirror which has to be moved in.

In the initial design, the Mistral instrument was supposed to be equipped with a wideband camera lens OB V-SWIR F100/2.0 from Optec SPA (<https://ir.optec.eu/pdf/C1602.pdf>). This camera lens had a coverage from 4000 to 17000 Å with a good MTF (> 40% @ 50 lp/mm). Unfortunately, the company was finally unwilling to produce a single lens for us and we did not find a reasonable cost alternative on the market. Lacking the time and budget to develop a custom lens, we opted to use two different commercial lenses to achieve full coverage of the 4000-10000 Å spectral band provided by the CCD camera, at the cost of a manual exchange needed to select the blue or the red setting. It is however planned in a second step to replace those two by a single one covering the full range with a good efficiency (see 2.6). The main characteristics are given in Fig.2 and Table 1.

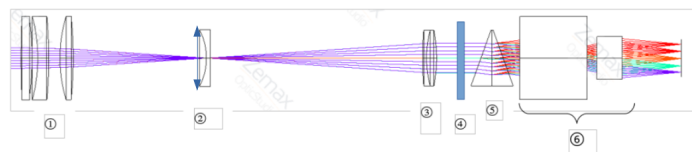


Fig. 2. MISTRAL optical scheme: (1) focal reducer, (2) field lens -128 mm (with the slit a few mm before), (3) achromat collimator f=200mm, (4) filter wheel, (5) VPH 600 tr/mm with two prisms 19,8° (blue)/25,6° (red), (6) 100mm lens

2.3. Observing modes and available spectral dispersors

Several observing modes (Table 2) are possible with MISTRAL, accessible from a dedicated Graphical User Interface (GUI hereafter), which shows the position of the different elements in the optical path. These are: the filters (with 12 positions), the spectral dispersors (blue and red VPH gratings, to be used with the blue or red camera lens respectively), and the slit (1.9 arcsec wide). These elements are summarized in Table 1 and selected according to the different operating modes (imaging, spectroscopy or set-up).

The dispersor (blue or red) has to be chosen before the beginning of the run in order for the right camera lens to be mounted during day time. This will change in the future, once a custom-made, wide spectral coverage, unique lens will be available, thus avoiding any dismantling of the instrument. In order to measure the CCD spectral response, several standard spectrophotometric stars were observed. Fig.3 shows the computed spectral response for the blue dispersor / blue lens from Feige 15 observations (Stone 1974a), and for the red dispersor / red lens from BD+26, 2606 observations (Oke & Gunn 1983). The total efficiency of the system (telescope + instrument + detector) is ~22% at the peak (6000 Å).

2.4. Exposure Time Calculators

Exposure time calculators are available remotely. One for spectroscopy: ETC1⁷ and one for imaging: ETC2⁸. The details of the

⁷ http://www.obs-hp.fr/guide/mistral/MISTRAL_ETC1.shtml

⁸ http://www.obs-hp.fr/guide/mistral/MISTRAL_ETC2.shtml

Table 1. Main characteristics of the MISTRAL instrument

Wavelength range	4100-8200 Å (blue setting) and 5800-9950 Å (red setting)
Spectral resolution	R~700@6000 Å, see also Section C
Fixed Slit Width	1.9arcsec
Optical efficiency (Telescope + spectrograph)	~0.22@6000 Å (mean OHP seeing of 2.5arcsec and slit of 2arcsec)
Imaging field of view	5.1arcmin full light (9arcmin in total)
Filter wheel	g', r', i', z', Y, H α , OIII, SII, H β , red and blue order separation filters
CCD	Andor iKon-L 936, 27.6x27.6 mm / 2048x2048 pxs of 13.5 μ , Deep Depletion CCD
Spectral Calibration lamps	Ar/Hg/Xe lamps for wavelength calibration, Tungsten for Flat Fields
Sampling	0.48arcsec for 13.5 microns pixels
Grism	Blue: Two prisms at 19.8° with VPH at 600 tr/mm @6000 Å d=50mm Red: Two prisms at 25.6° with VPH at 600 tr/mm @9000 Å d=50mm
Camera lenses	Blue: Nikon AF-S 100mm F/1.4 Red: XENON-EMERALD 2.9/100-L

Table 2. Main MISTRAL modes: (1): To measure the electronic offset signal. (2): To center targets in the image (imaging mode), and to focus the telescope. Fast reading with relatively high reading noise. These images are not saved. (3): To take science images. (4): To take flat field images, to correct the pixel to pixel differential response. This has to be done preferentially on the sky (see below), and for each filter, as the response is very different from one filter to another one. (5): To locate the slit “x” position on the CCD before moving the telescope to then center the target within the slit. The slit is seen thanks to the sky surface brightness. Rapid reading mode. (6): To move the target at the slit position. Rapid reading mode. Images are not saved. (7): To take the spectrum of your science target (blue or red disperser). In principle to be done without other filters in the beam (but can be done if you have a special reason to do it), and with an order separation filter for the red disperser. (8): To take wavelength spectral calibrations in order to transform the “x” position into wavelength. (9): To take spectral flat fields to correct for CCD differential pixel to pixel response.

Mode	Shutter	Reading mode	Dispersor	Slit	Calib. mirror	Wave. calib. lamp	Spectral flat field lamp
(1)Bias	Closed	50 kHz	N/A	N/A	Off	Off	Off
(2)Preview Image	Open	3 Mhz	Off	Off	Off	Off	Off
(3)Science Image	Open	50 kHz	Off	Off	Off	Off	Off
(4)Imaging Flats	Open	50 kHz	Off	Off	Off	Off	Off
(5)Search Slit Position	Open	3 Mhz	Off	On	Off	Off	Off
(6)Centering on the slit	Open	3 Mhz	Off	Off	Off	Off	Off
(7)Science Spectrum	Open	50 kHz	On	On	Off	Off	Off
(8)Calibration Arc	Open	50 kHz	On	On	On	On	Off
(9)Calibration Tungsten	Open	50 kHz	On	On	On	Off	On

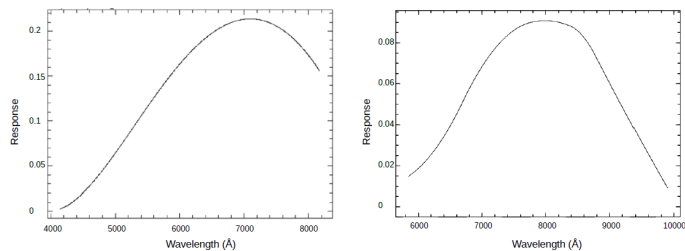


Fig. 3. Relative spectral response over the CCD 4000-10000 Å range. Left: blue dispersor / blue lens (from Feige 15 observations). Right: red dispersor / red lens (from BD+26,2606 observations).

needed parameters to enter into the calculators are described in the Appendix A, and some results are displayed there also. Here, we only give a quick flavor of what can be achieved.

For spectroscopy, we summarize in Table 3 the V band magnitudes detected with a total exposure time of 1 hour, with a S/N of 3, for point-like objects, under a median seeing (for OHP) of 2.5 arcsec, and with moon conditions: 135° from moon, 25% illumination.

For imaging, ETC2 gives the exposure time needed to detect objects at a given magnitude with the requested S/N. While the details of the procedure are fully described in the Appendix, we summarize the important results in Table 4.

See also http://www.obs-hp.fr/guide/mistral/CookBook_main.pdf (page 23) for the minimal possible exposure times.

2.5. Data Archival

In addition to their local storage in the MISTRAL computers at the telescope, raw MISTRAL data are automatically archived within a database⁹ hosted by the CeSAM¹⁰. Raw data are visible but not accessible during a proprietary period of 12 months to people other than principal investigators. All calibration data are immediately public. A possibility is also offered to the observers to store/make available their final reduced data and added values through the GASPIC national service¹¹.

2.6. Expected optical improvement

In order to increase the instrument’s efficiency, and avoid change-overs of optics when changing from blue to red settings (or vice-versa), we are preparing a single camera lens covering the full MISTRAL spectral range: it is expected to be installed on the instrument in 2024/2025.

⁹ <https://data.lam.fr/mistral/home>

¹⁰ <https://www.lam.fr/service/cesam/preentation/>

¹¹ <https://gaspic.osupytheas.fr>

Table 3. Typical spectroscopic limiting magnitudes corresponding to a total exposure time of 1 hour, with a S/N of 3, for point-like objects, under a median seeing of 2.5 arcsec, and with moon conditions: 135° from moon, 25% illumination. Values are given for pure absorption line spectra (blue dispersor), pure absorption line spectra (red dispersor), emission line spectra (blue dispersor), and emission line spectra (red dispersor)

	Abs. lines Blue dispersor	Abs. lines Red dispersor	Em. Lines Blue dispersor	Em. Lines Red dispersor
V magnitude	≤19.5	≤19.5	≤20.5	≤20

Table 4. 90% completeness for point sources under average imaging observing conditions at OHP.

g'	20min: g'~20.5
r'	10min: r'~20.
i'	10min: i'~21.
z'	10min: z'~19.5
Y	10min: Y _{AB} ~18.5

The new, custom-made camera design consists of 5 lenses with 2 aspheric surfaces and uses low-dispersion OHARA S-FPL53 glass for the strong positive lenses. It is optimized to operate in the full working spectral range with a dispersed beam, which implies a forward-shifted entrance pupil.

The expected performances of the lens in development are compared to those of the commercial lenses which are currently used in the instrument. In the actual blue-visible setting, an FX AF-S NIKKOR 105mm f/1.4 lens is used and its module transfer function (MTF hereafter) is available from the manufacturer at two reference spatial frequencies. In order to make a correct comparison, the calculations in the visible were made for the F , d and C wavelengths (4860-6560 Å) and the field edge corresponds to 11° in each case. As the throughput curve for this Nikon lens is not available, it was estimated from the known number of surfaces and groups in the design, presuming that the anti-reflective (AR) coating has a residual reflectance of 1% (similar to that in the custom design, see also http://www.obs-hp.fr/guide/mistral/CookBook_main.pdf (page 20) and the glass types composition is close to that used in [U.S.Patent 5572277]. The commercial lens data are taken from the [www](http://www.12)¹². It comes out that the throughput increases from about 75% to about 95% at 5000, 6000 or 7000 Å and markedly from 19% to 77% at 4000 Å, while the MTF is only marginally decreasing.

In the same way the comparison was done for the Schneider Emerald 2.9/100 F-LD lens, which is actually used in the red range. This time both the MTF and throughput are known from the product's datasheet¹³. Here the foreseen transmission is similar with the present one at 7000 Å (93%), and slightly lower at 8000 Å (90% instead of 95%), with a few percent decrease of the MTF at 40l/mm. However, it should also be noticed that the aperture of the current Schneider lens is insufficient and results in significant vignetting towards the edges of the spectrum, with a maximum loss of 40% at 6000 Å and 10000 Å. Thus, this vignetting loss will disappear with the new camera lens.

Note that the nominal f-number, design wavebands and the pupil positions are different for all these lenses, so the comparison is not straightforward. However, it indicates that the custom design is notable for an increased throughput in the shortwave

visible range and the contrast at mid-spatial frequencies remains high even for a faster beam.

3. On-sky validations

In order to give to the reader a real-life idea of what is possible with MISTRAL, we report now salient (unpublished) examples of science done with MISTRAL observations during its first two years of exploitation. Following the main science goals of the instrument, as described in the introduction, various types of objects were observed during several test periods, starting in April 2021 and lasting until around end of 2022, with progressively more science taking over the tests themselves. We describe below some of the results obtained so far.

We give in Table 5 the observing conditions of the spectra shown in Figures 4, 5, 6, and 10.

3.1. Emission lines stars: example of NovaCas 2021

V1405 Cas was discovered on March, 18th 2021 and could be observed during the first commissioning nights of the instrument, in April and July 2021. For instance, the spectra obtained on July 5th, 2021 (that is about 100 days after maximum), still showed PCygni profiles in the H and He Balmer lines, sign of the expanding envelope, but also some NII lines and some FeII lines, indicating that the object was transiting from the He/N phase to the FeII phase. In Figure 4 we show two spectra of this slow Nova, observed later with both the blue and red MISTRAL grisms, on June 30th, and June 28th, 2022, respectively, that is about 415 days after maximum. The PCygni profiles do not appear anymore in those spectra, and the line profiles do not show yet a rectangular shape either, confirming the fact that we deal with an FeII type. The linewidths of the strong lines are measured at 1800 km/s FWHM. Besides the lines of H and He, most conspicuous are the strong lines of [FeVII], in particular those at 6086 and 5721 Å. On the other hand, the absence of the usually strong OI lines 8446 Å (and the less strong 7773 Å) is surprising: we have to wait that the Nova has reached the full nebular phase to make a proper abundance analysis.

3.2. General stellar classification: bow shock stars

Bow-shocks (BS) are arc-shaped structures located ahead of a star and generally observed at mid-to-far IR wavelength. They are expected to result from the interaction of the stellar wind with the ambient interstellar medium (ISM) when the star has a relative supersonic motion respectively to the ambient medium. Because the bow-shock driving star is expected to be a O or B type star we led a spectroscopic follow-up of a sample of 47 bow-shock stellar candidates selected from the Jayasinghe et al. (2019) catalog and selected to be observable with the MISTRAL instrument. Figure 5 shows a typical spectrum for a $V=9.7$ star.

The spectral classification of stars is commonly done from lines in the 4000-5000 Å domain but, due to the lower sensitivity of the instrument in this spectral range, we performed the

¹² <https://photographylife.com/lenses/nikon-af-s-nikkor-105mm-f1-4e-ed/3>

¹³ https://schneiderkreuznach.com/application/files/3316/4725/4957/EMERALD_29_100_F-LD_1070506_datasheet.pdf

Table 5. Observing details for the targets described in section 3. Moon illumination is given in percentage along with the distance to the target in degrees.

Target Name	Observation Date	Seeing (arcsec)	Moon	Exposure Time	Air Mass	Dispensor
NovaCass 2021	29/06/2022	3.0	1% @ 80°	2×600sec	1.2	red
NovaCass 2021	01/07/2022	5.1	4% @ 86°	1×800sec	1.1	blue
LkH α 324SE	08/12/2021	3.2	26% @ 72°	2×900sec	1.2	red
2G1045666+0128085	02/07/2022	2.2	8% @ 98°	1×900sec	1.05	blue
C/2022 E3 (ZTF)	10/02/2023	1.9	78% @ 123°	10×240sec + 2×120sec	1.1	blue

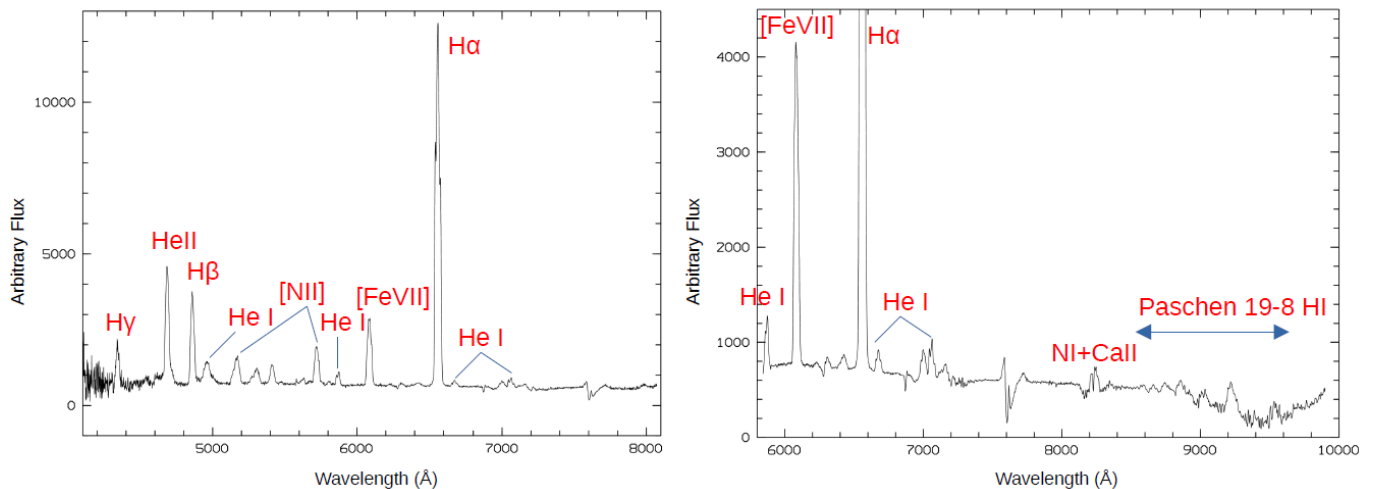


Fig. 4. Spectra of V1405Cas = NovaCas2021, obtained in June 2022, with the blue setting (left) and the red setting (right, enhanced y scale).

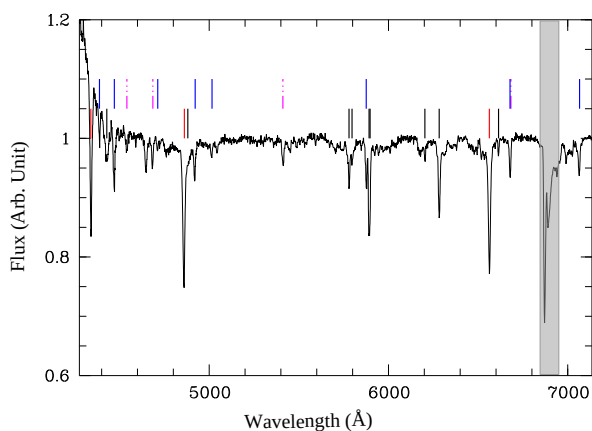


Fig. 5. Continuum normalised spectrum observed with MISTRAL of the candidate BS star 2G1045666+0128085. The position of the main lines used for the classification (magenta, blue, and red dashes correspond to HeII, HeI and Balmer lines respectively) and the diffuse interstellar bands (black dashes) are indicated. The grey vertical band underlines the night-sky feature.

spectral classification from lines in the red part (4500-7000 Å) of the spectrum (Mk standards in the red have been provided by, e.g. Danks & Dennefeld (1994)). We find that among the 47 candidates we have: 2 unclassifiable stars, 3 cool stars, 1 A-type star, 10 O stars and 31 B (mainly giants and super-giants) stars which allows us to confirm that bow-shocks are mainly driven by hot stars. The details of these results, complemented with transverse velocity study (based on Gaia-DR3 astrometric data) of the stars, can be found in Russeil et al. (in preparation).

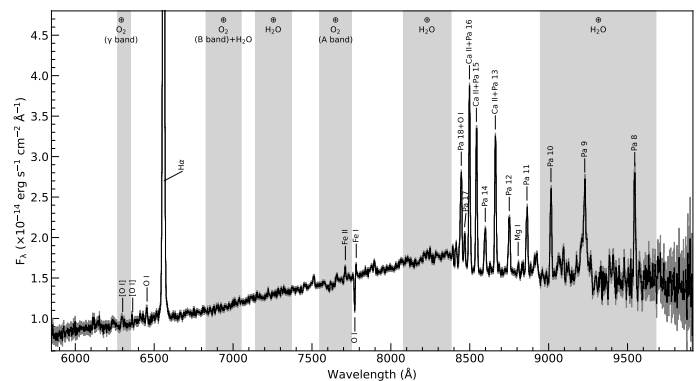


Fig. 6. MISTRAL spectrum of LkH α 324SE with telluric corrections, obtained with the red configuration and a single exposure of 900 s (among the two observed) on the night of 2021 Dec. 8. The flux error-bars are plotted in gray. The vertical light-gray stripes indicate the atmospheric absorption bands of water and molecular oxygen.

3.3. The red domain towards 1 μ : the variable, pre-main sequence star LkH α 324SE in Lynds 988

Gaia21fji¹⁴ (a.k.a. AT2021aftk¹⁵ in the IAU designation) was reported on 2021 Nov. 6 as the "brightening of a variable red Gaia source, candidate YSO" (Hodgkin et al. 2021). We obtained a classification spectrum on 2021 Dec. 8 with MISTRAL in the red configuration (Adami et al. 2021). In fact, Gaia21fji corresponds to the emission-line star LkH α 324SE (Herbig & Rao 1972; Chavarría et al. 1983; a.k.a. HBC 727 in Herbig & Bell

¹⁴ <http://gsaweb.ast.cam.ac.uk/alerts/alert/Gaia21fji/>

¹⁵ <https://www.wis-tns.org/object/2021aftk/discovery-cert>

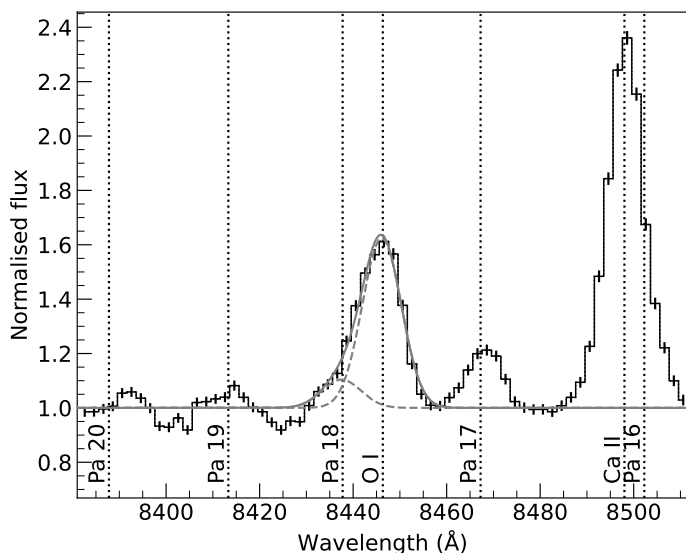


Fig. 7. Pa 18 $\lambda 8437.75$ and O I $\lambda 8446.76$ from LkH α 324SE. The grey solid line is the combined Gaussian best-fit of these two lines. The grey dashed lines are the individual Gaussian best-fits of these two lines, confirming the detection of the Pa 18 line (see text for details).

1988), which is a member of the pre-main sequence population of the dark cloud Lynds 988 located at ~ 600 pc (Herbig & Dahm 2006), therefore, it is not a new candidate YSO identified by Gaia. The spectrophotometric standard Feige 15 was observed after LkH α 324SE (Appendix D).

The spectrum displays many strong emission lines above a red continuum (Fig. 6): H α , Paschen (Pa) lines, the Ca II infrared triplet (IRT), and the O I $\lambda 8446$. Fainter emission lines of Mg I, Fe I, and Fe II are also detected, plus forbidden O I lines. The O I $\lambda 7772$ absorption triplet is detected. The Ca II IRT in emission is an indicator of chromospheric activity and potentially of accretion (Mohanty et al. 2005; Yamashita et al. 2020).

The emission lines Pa 8–12, 14 and 17 are detected. Pa 8–10 are located in the MISTRAL spectrum region that is strongly affected by the fringing (see also http://www.obs-hp.fr/guide/mistral/CookBook_main.pdf page 16 and http://www.obs-hp.fr/guide/mistral/Test_report.pdf page 15) and the water absorption-band, therefore, the measured equivalent widths (EW hereafter) could be sensitive to the determination of the pseudo-continuum and the correction of the telluric absorption. Pa 16 $\lambda 8502.27$, Pa 15 $\lambda 8545.17$, and Pa 13 $\lambda 8664.80$ cannot be resolved with MISTRAL from the emission lines $\lambda \lambda 8498.02$, 8542.09 , 8662.14 , respectively, of the Ca II IRT (see bottom panel of Fig. C.1). However, Pa 18 $\lambda 8437.75$ and O I $\lambda 8446.76$ are 9.01 \AA apart, which is just large enough to be barely resolved as MISTRAL FWHM is 8.5 \AA at this wavelength (see bottom panel of Fig. C.1). Fig. 7 shows the MISTRAL spectrum centered on the O I $\lambda 8446.76$ with a hint of Pa 18 on its red wing.

Herbig & Dahm (2006) have also identified the [S II], [O I], and [N II] lines from LkH α 324SE; the [O I] $\lambda \lambda 6300$, 6363 lines have the same shape than the [S II] $\lambda \lambda 6717$, 6730 lines, which display a narrow component at -18 km s^{-1} superposed to a very broad asymmetric line peaking near -200 km s^{-1} (their Fig. 12, bottom panel). The [O I] high- and low-velocity components of T Tauri stars are associated to micro-jet and disk wind, respectively (Hartigan et al. 1995). The [N II] $\lambda \lambda 6548$, 6583 lines cannot be resolved with MISTRAL from the broad wings of the H α line. The [S II] $\lambda \lambda 6717$, 6730 lines are not detected with MIS-

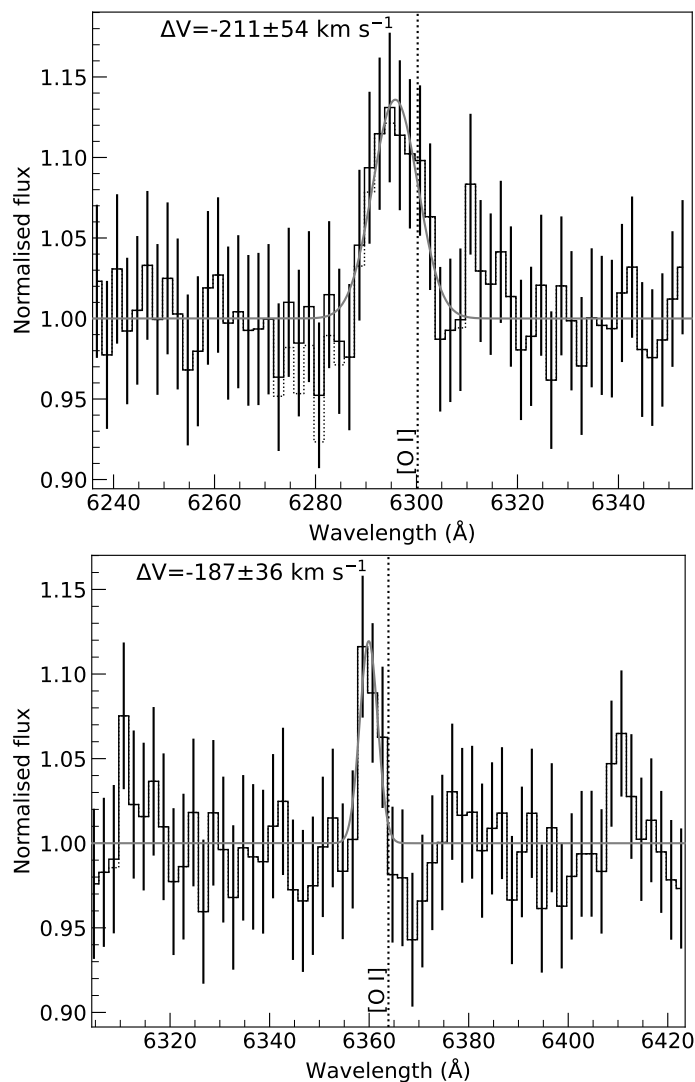


Fig. 8. Faint, blueshifted [O I] emission lines from LkH α 324SE. In the top panel, the dotted step line is the normalised spectrum with no correction of the atmospheric O $_2$ γ band. The gray line is the Gaussian fit. The quoted error of the velocity shift includes quadratically the wavelength calibration error.

TRAL, but our $1.9''$ -slit was oriented NS, not at position angle of 309° along the NW flow as in Herbig & Dahm (2006), which may dilute the observed flux from the base of the NW flow. Fig. 8 shows the regions of the [O I] $\lambda \lambda 6300.23$, 6363.88 lines with two faint emission lines with EW of -1.6 and -0.3 \AA , respectively. These faint lines are blueshifted, with velocity shifts that are consistent with the high-velocity, broader component of these lines. Therefore, MISTRAL can also detect faint forbidden [O I] lines from this pre-main sequence star.

3.4. Test of the MISTRAL spectral resolution around the H α line in LkH α 324SE

In MISTRAL's observations of LkH α 324SE, the H α line is strong with an EW of -107 \AA , which is well above the maximum H α EW of -20 \AA that can be produced by active stellar chromosphere in later M spectral-type, therefore, the origin of this emission is from accretion shock at the stellar surface (Muzerolle et al. 2001). Moreover, the H α line is broad with $\text{FWHM}(\text{H}\alpha) = 13.98 \pm 0.05 \text{ \AA}$ (Fig. 9), which is well larger than

MISTRAL's spectral resolution of 7.9 \AA for the red configuration (Appendix Eq. C.2). The (deconvolved) full width at 10% of the $H\alpha$ peak is $961 \pm 5 \text{ km s}^{-1}$ (Appendix Eq. C.3), which is larger than the minimum value of 270 km s^{-1} used as accretion criteria in low-mass stars (White & Basri 2003). We note small residuals between the MISTRAL $H\alpha$ line and the Gaussian fit that suggest for this line an asymmetric profile. Indeed, the high-resolution ($R \sim 45,000$) spectra of Lk $H\alpha$ 324SE, obtained on 2003 Jul. 6 and Dec. 13 with the HIRES spectrograph at the Keck I telescope on Mauna Kea, shows the $H\alpha$ line (Fig. 10, top panel of Herbig & Dahm 2006) with an EW of -170 \AA , wings extending to at least $\pm 550 \text{ km s}^{-1}$, and an absorption component at -114 km s^{-1} , usually associated with a stellar wind, between the secondary and main line-peaks at -200 and 2 km s^{-1} , respectively. We note that the secondary peak is less than half the strength of the primary peak, classifying this $H\alpha$ line as a type IIIB profile, which is the most common (33%) in T Tauri stars, whereas it is three times less common (11%) in Herbig Ae/Be stars (Reipurth et al. 1996).

A medium-resolution ($R=5,000$) spectrum in the blue of Lk $H\alpha$ 324SE was obtained by C.A. 12 days after the MISTRAL observation on the night of 2021 Dec. 20, with the AURELIE spectrograph at the OHP 1.52m telescope (Gillet et al. 1994). This AURELIE spectrum will be reported elsewhere. Here, we focus only on the $H\alpha$ line observed with AURELIE (Fig. 9). This type IIIB-profile line displays: an EW of -119 \AA , i.e., 43% fainter and 10% stronger than during the HIRES and MISTRAL, respectively, observations; the absorption component at -52 km s^{-1} , i.e., twice-less blueshifted than observed 18 years before; the secondary and main line-peaks at -174 and 112 km s^{-1} , respectively, i.e., less blueshifted and much more redshifted, respectively, than observed 18 years before. The $I_{\text{max}}/40$ velocities (Reipurth et al. 1996) for the blue and red wings are -507 and 601 km s^{-1} , respectively. We use the shape of the AURELIE $H\alpha$ line as template for comparison with the MISTRAL $H\alpha$ line. After convoluting (Gaussian with $\sigma = 3.3 \text{ \AA}$ from quadratic combination of resolution) and resampling (2 \AA spectral-bins) this template, the best-fit match with the MISTRAL $H\alpha$ line is obtained for a velocity shift of about -227 km s^{-1} . However, this large value of the required velocity shift suggests on the timescale of 12 days a strong variation of the shape of the $H\alpha$ line, including for instance, a more blueshifted absorption component during the MISTRAL observation.

3.5. Solar System objects: the C/2022 E3 (ZTF) comet

The bright comet C/2022 E3 (ZTF) was observed in manual tracking mode for two exposure times, 120s and 240s, using the MISTRAL spectrograph camera on the 1.93 m OHP telescope on February 10th, 2023, when the comet was at a distance of 1.20 AU from the Sun and 0.39 AU from the Earth. We used the blue mode covering the $\sim 4200\text{-}8000 \text{ \AA}$ range at resolution ~ 750 with a 1.9arcsec width slit. All the acquired frames for different exposures were bias subtracted and then flat fielded using the spectral flat lamp present in the instrument (Tungsten). The cosmic rays were removed using the LACOSMIC package (van Dokkum 2001). The reduced and extracted 1D spectrum is shown in Fig.10.

Both the 120s and 240s spectra, even if slightly trailed, were used to compute the production rates of C2 ($\Delta\nu = 0$) emission band using a single aperture (200 pixel aperture) with the comet at the centre, as mentioned in Aravind et al. (2021). The 120s spectra that were better guided with a narrower dust continuum

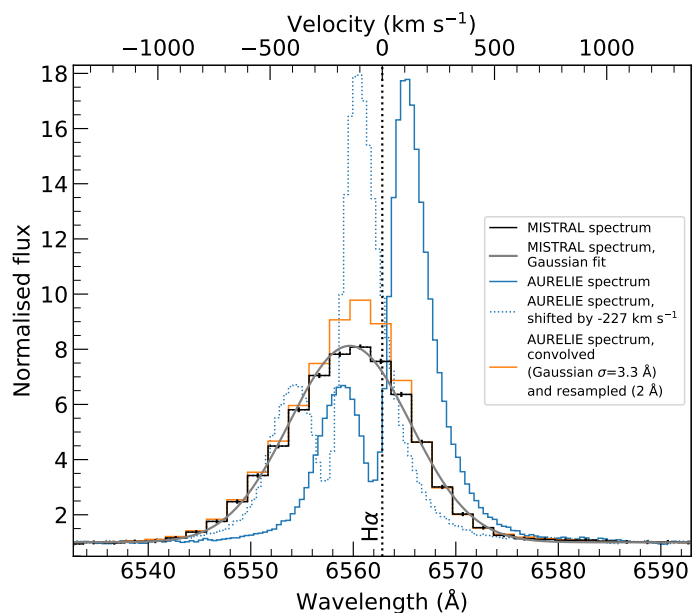


Fig. 9. Broad and variable, $H\alpha$ emission line from Lk $H\alpha$ 324SE. The black data with error bars are the normalised MISTRAL spectrum. The grey line is the Gaussian fit of the emission line. The solid blue line is the medium-resolution ($R \sim 5,000$) spectrum obtained, 12 days after the MISTRAL observations, with the OHP 1.52m telescope with the AURELIE spectrograph. The dotted blue line is the same spectrum shifted by -227 km s^{-1} to match the position of the emission line observed with MISTRAL. The orange line is the convolved (Gaussian with $\sigma = 3.3 \text{ \AA}$) and resampled (2 \AA spectral bins) AURELIE spectrum to match MISTRAL spectral resolution and sampling.

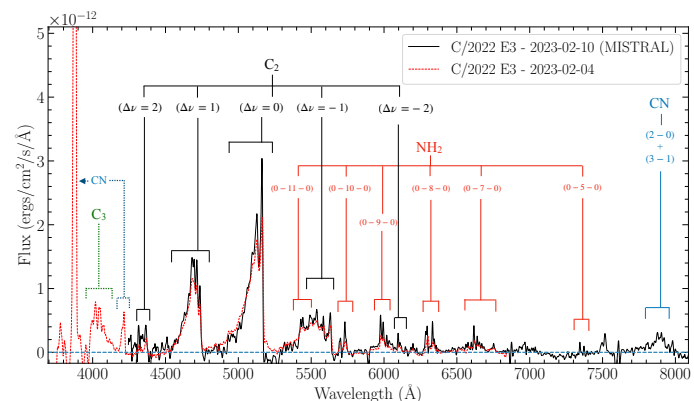


Fig. 10. Black line: optical spectrum of comet C/2022 E3 (ZTF) observed using the MISTRAL spectrograph camera on the OHP telescope. The spectra, obtained from the 240s frame, was extracted using a $29.2\text{arcsec} \times 1.93\text{arcsec}$ aperture with the comet at the centre. Red dashed-line: spectrum obtained from the HCT telescope (private communication).

were used to extract spectra with apertures of equal widths moving away from the photo centre to compute spatial profile of the column density and hence the production rates with the help of Haser (1957) modelling. The spectrophotometric standard, Hiltner600, observed on the same night using the same configuration was used to produce the sensitivity curve of the instrument and then flux calibrate the comet spectra. The Solar analog standard star HD19445 was observed on the same night to remove the dust reflected solar continuum present in the optical spectra. Even though, ideally, a separate sky frame of similar exposure is required to remove the sky background from the comet frames,

we used the sky from a point source observed with a similar exposure time on the same night to remove the sky lines.

Several usual cometary emission bands were detected from C2, NH₂ and CN radicals. The production rate of (2.61+/-0.04)E26 and (2.51+/-0.07)E26 for C2 ($\Delta\nu = 0$) were computed for the 240s frame and 120s respectively and are in good agreement with the values reported for the same comet from the TRAPPIST telescopes ((Jehin et al. 2022); ATel 15822). The $A_{f\rho}$, a proxy to the dust production (A’Hearn et al. 1984) computed for the green continuum narrow band filter (Farnham et al. 2000), from spectroscopic data using techniques as mentioned in (Aravind et al. 2022), was found to be around 5100±80 cm, which is again in agreement with the values reported from TRAPPIST for the comet at similar observational epochs.

As a comparison, we also show in Fig.10 the spectrum obtained for comet C/2022 E3 from the 2 meters class Himalayan Chandra telescope (HCT, private communication). This telescope is using the Hanle Faint Object Spectrograph and Camera (HFOSC) and covers a wavelength range of 3750-6850 Å. The comparison shows the nice resolution of MISTRAL showing the emission lines in a sharper way. MISTRAL is also going deeper in the red but is also missing the blue part of the spectrum with the bright CN line, well visible in the HCT spectrum. This, e.g., justify the new lens we are developing, more efficient toward the blue.

With the help of these OHP observations, the MISTRAL spectrograph camera on the OHP telescope proves to be reliable for cometary observations for a wavelength range of 4200 Å - 8000 Å. With proper differential tracking and required frames acquired in an orderly manner, longer exposure observation of fainter and more distant comets could be used to effectively analyse the column density profiles of the various emission bands marked in the figure, which can further be used to compute their production rates.

4. Main targets of MISTRAL: the GRB follow-up program

The MISTRAL instrument is well-suited for studying the GRB physics (see e.g. Schneider et al. (2023b)) as it combines both a low-resolution spectroscopic mode (with a blue and red range) sufficient to infer their redshift using absorption lines in the afterglow emission, and an imaging mode that allows to characterize their optical and NIR temporal evolution. The French GRB community has proposed a dedicated MISTRAL ToO program in order to characterize the afterglow emission of the well-localized bursts detected by the BAT and XRT high-energy instruments on board the *Neil Gehrels Swift* space observatory (Gehrels et al. 2004). This program is preparatory for the future exploitation of the Sino-French *SVOM* mission expected to be launched in June 2024 (Wei et al. 2016), and has been conducted since March 2022.

We have presently strict trigger criteria to avoid disturbing too much the other observing programs, but in practice, they can be relaxed for important events (e.g. following information reported by other teams via Gamma-ray Coordination Network (GCN) circulars¹⁶) and will need to be revised once *SVOM* will be in operations. So far, we have observed 21 GRBs as shown in Table 6.

Most of the observed GRBs in Table 6 were day-time triggers explaining the relatively long delay between trigger and MISTRAL observations. This is due to the pointing strategy of the

Swift spacecraft that can detect bursts near the Sun direction. On the contrary, *SVOM* has an optimized anti-solar pointing strategy which will result in detecting GRBs only during the night time on Earth and thus will enhance the rates of fast follow-up at the OHP site. Few GRBs were observed with very long latency (GRB 221009A and AT2023lcr) because newly received information (updated position and flux measurements) allowed us to identify these events as interesting targets. For now, the only (Swift) night-time trigger was GRB 240218A, which we were able to observe 30 min after the alert. We could in principle be faster, but the telescope rules impose to finish the exposure of the ongoing regular observing program if less than 30 minutes are remaining. This therefore mechanically limits the reaction time to ~30minutes.

4.1. Data analysis

For each GRB MISTRAL ToO, we start with a typical sequence of r-band images in order to detect the source and then to accurately place the slit at the right GRB location. If the GRB remains too faint or undetected after these first images we keep observing in imaging mode to reach a higher sensitivity. If the GRB is detected and bright enough as compared to the MISTRAL spectroscopic limiting magnitude ($r < 19 - 20$), we perform spectroscopic observation for about 1 hour to obtain a good S/N s6). Table B.1: It is recommended to draw the profiles of the filters followed this table. spectrum of the source. Both the photometric and spectroscopic data are reduced immediately in order to communicate our results in real time to the scientific community.

4.2. Data reduction

We first pre-process the MISTRAL raw images with the appropriate bias and flat field calibration images. The single exposure images are then astrometrically solved and coadded to be analyzed. The GRB positions were known at the arcsecond level of accuracy which allows us to directly perform forced photometry. To do so, we used the Simple Transient Detection Pipeline, STDPipe, (Karpov 2021). Our photometric analysis followed the steps described below (and in the git documentation¹⁷ of the STDPipe project):

1. We mask the saturated stars, the cosmic ray artifacts and the bad columns of pixels
2. We extract the point-like sources (S/N>3) using SExtractor (Bertin & Arnouts 1996).
3. We calibrate the photometry of the sources using the PHOTUTILS¹⁸ Astropy package (Bradley et al. 2021). We use the PanSTARRS DR1 catalog (Chambers et al. 2016) as a reference, a crossmatch radius of 2 arcseconds to associate the cataloged sources to our SExtractor ones, and a flux aperture radius $\sim 1.5 \times \text{FWHM}$ (the mean of the full width at half maximum of the image sources). The local background was measured in an annulus of $[3-5] \times \text{FWHM}$
4. To reduce the flux contamination from nearby sources or the GRB host galaxy (if visible in the images), we may perform a difference image analysis using the HOTPANTS code (Becker 2015) and the the CDS HiPS2FITS service (Boch et al. 2020)
5. If the source is detected in the coadded image, we perform the forced aperture photometry at the GRB localization using the same aperture configuration as during the calibration steps

¹⁷ <https://stdpipe.readthedocs.io/en/latest/index.html>

¹⁸ <https://github.com/astropy/photutils>

¹⁶ <https://gcn.nasa.gov/circulars/>

Table 6. The list of the GRBs followed up at OHP using the MISTRAL instrument mounted on the 193cm telescope during the semesters 2022A, 2022B, 2023A and 2023B.

GRB name	mode	setting	Exp time sec	detection	mag	$T_{\text{obs}} - T_{\text{GRB}}$ hours	MISTRAL redshift	GCN Circ.
220623A	imaging	red	3300	No	$i \geq 21.5$	15.2	–	Schneider et al. (2022b)
220708B	imaging	blue	3600	No	$r \geq 22.3$	19.5	–	Turpin et al. (2022)
220711B	imaging	blue	3000	No	$r \geq 21.3$	3.1	–	–
221009A	imaging	blue	1800	Yes	$i = 20.09$	78	–	Schneider et al. (2022a)
230205A	imaging	blue	640	No	$r \geq 20.95$	17.8	–	Turpin et al. (2023a)
230328B	imaging	blue	3000	Yes	$R_c = 20.03$	4.5	–	Adami et al. (2023i)
230409B	imaging	blue	1800	No	$i \geq 20.6$	22.3	–	Adami et al. (2023h)
230427A	imaging spectro	blue	4920	No	$r \geq 22.3$	11.3	–	Turpin et al. (2023c) Adami et al. (2023e)
230506C	imaging spectro	blue	1800	Yes	$r = 20.9$	3.8 4.4	$3.7 \leq z \leq 4$	Adami et al. (2023c) Adami et al. (2023g)
230510A	imaging	blue	4200	Yes	$r = 21.8$	13.2	–	Schneider et al. (2023a)
AT2023lcr	imaging	blue	4560	Yes	$r = 20.84$	44.4	–	Adami et al. (2023j)
230723B	imaging	blue	3420	No	$r \geq 21.$	10.0	–	Adami et al. (2023d)
230805B	imaging	blue	3000	No	$r \geq 21.5$	9.7	–	Turpin et al. (2023d)
230812B	imaging	blue	1260	Yes	$r = 20.32$	25	–	Adami et al. (2023a)
			1200		$r = 22.36$	120		Adami et al. (2023b)
			2400		$r = 22.37$	145		Adami et al. (2023b)
			5500		$r = 22.45$	169		Adami et al. (2023b)
			7200		$r = 22.37$	241		Amram et al. (2023)
AT2023sva	imaging spectro	blue	900 5400	Yes	$r = 20.96$	–	$z < 3.5$	Parra-Ramos et al. (2023)
231205B	imaging	blue	4620	No	$r \geq 20.65$	5.2	–	Adami et al. (2023f)
231215A	imaging	blue	3000	Yes	$r = 21.32$	7.4	–	Turpin et al. (2023b)
231216A	imaging	blue	3000	No	$r \geq 22.2$	3.0	–	Basa et al. (2023)
240204A	imaging	blue	16200	Yes	$r = 21.82$	4.1	–	Adami et al. (in press)
240209A	imaging	blue	1800	Yes	$r = 20.06$	4.9	–	Turpin et al. (in press)
240218A	imaging	blue	3600	No	$r \geq 23.0$	0.5	–	Adami et al. (in press)

6. If the source is not detected, we estimate the upper limit from the local background for a source that would have given a positive detection at a given S/N

For spectroscopy, we used the night-time dedicated MISTRAL spectroscopic pipeline¹⁹ which is based on the ASPIRED (Lam et al. 2023) software.

4.3. Results

For 9/21 (~ 45%) of our follow-up campaigns, we were able to clearly identify and measure the brightness of the GRB afterglows. Note that among them, we detected AT2023sva (Parra-Ramos et al. 2023), a GRB afterglow without any high-energy trigger that was initially discovered in ZTF survey data from blind searches for fast optical transients (Vail et al. 2023). We also covered several observational epochs both for the brightest GRB of all time (the "BOAT"), GRB 221009A, and for the third brightest Fermi-GBM burst, GRB 230812B (OHP data reported in Hussenot-Desenonges et al. 2023). Section 4.4 describes in more detail our photometric results for GRB 221009A.

In addition, we were able to trigger four times the spectroscopic mode of MISTRAL to characterise the transient or to infer the redshift of the potential host galaxy for GRB 230427A (Adami et al. 2023e), for GRB 230506C (Adami et al. 2023c) and for the orphan afterglow AT2023sva (Parra-Ramos et al.

2023). For the GRB 230506C, we suggest a redshift of $3.7 \leq z \leq 4$, the only redshift measurement reported for this burst, which also represents the most distant redshift measured at OHP so far. The spectrum of GRB 230506C showcases the capabilities of MISTRAL pushed to its limits, securing a tentative spectroscopic redshift measurement for a source at magnitude $r \sim 20.9$ with a 30min total exposure time (blue dispersor). The redshift was determined taking advantage of a break present around 6000 Å that was interpreted as the Lyman- α break (see Fig. 12). For the 12/21 non-detected GRBs, we were able to put interesting constraints on their optical flux evolution as shown in Figure 11 in the r-band.

4.4. GRB 221009A: the "BOAT"

GRB 221009A was triggered by the Gamma-ray Burst Monitor (GBM) instrument onboard *Fermi* (Veres et al. 2022; Lesage et al. 2023). It has been then detected during days to weeks at all wavelengths including at TeV energies (Fulton et al. 2023; Laskar et al. 2023; Williams et al. 2023; Aharonian et al. 2023; Levan et al. 2023; An et al. 2023; Kann et al. 2023; Cao et al. 2023). It was rapidly established that the properties of this burst were extraordinary given its intense luminosity and close distance (i.e. $z = 0.151$ Malesani et al. 2023). Many aspects of the GRB 221009A physics regarding the nature of the GRB relativistic jet and its angular structure, the efficiency of the jet's kinetic to radiation conversion mechanisms and the afterglow radiation model (Gill & Granot 2023; Zheng et al. 2023; O'Connor

¹⁹ http://www.obs-hp.fr/guide/mistral/MISTRAL_spectrograph_camera.shtml#H5

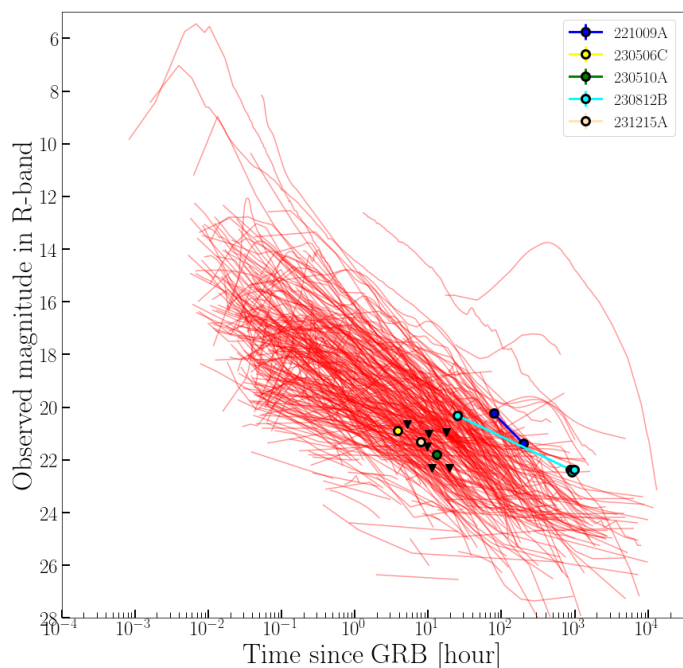


Fig. 11. Comparison of the MISTRAL GRB afterglow detections (colored circles) and upper limits (black triangles) with respect to the known population of GRB afterglows (1997-2023: not a complete sample)

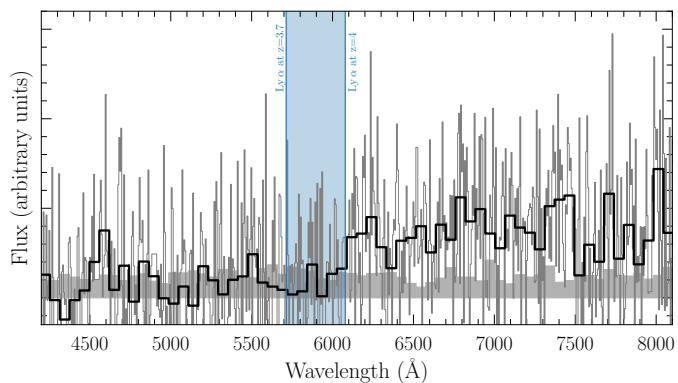


Fig. 12. Spectrum of GRB230506C taken by MISTRAL (30min exposure). The thin black curve represents the full spectrum while the thick black curve represents the spectrum rebinned by 20 pixels; the gray shaded area represents the error spectrum. The center of the expected Ly α positions for $z = 3.7$ and $z = 4$ are shown as the blue vertical lines; the blue shaded area represents the possible values of the Ly α centroid, assuming the drop at 6100 \AA is due to Lyman break.

et al. 2023; Ren et al. 2023; Zhang et al. 2023; Dai et al. 2023), or the Lorentz invariance principle (Vardanyan et al. 2022; Finke & Razzaque 2023; Piran & Ofengeim 2023; Yang et al. 2023), have been highly debated in the scientific community. These discussions will continue in the upcoming months/years as such an event is believed to occur only once every 10,000 years (Burns et al. 2023) and is therefore a rare opportunity to study the GRB physics with great details. In this very active context, we have performed two epochs of photometric observations at about 6 and 10 days after the *Fermi*-GBM trigger time, complemented with three epochs with the 120cm telescope at OHP (Schneider et al. 2022a). In Table 7, we summarized our photometric results and showed them in the context of the worldwide follow-up campaigns in Figure 13.

Table 7. Optical and NIR observation of GRB 221009A with the T193/MISTRAL and T120 telescopes located at OHP. The reported magnitudes are not corrected for the significant galactic extinction $E(B-V) = 1.32 \text{ mag}$.

$T - T_{GRB}$ (days)	filter	facility	magnitude (AB)
3.259	i'	T120	19.14 ± 0.08
3.273	r'	T120	20.23 ± 0.09
3.296	z'	T120	18.35 ± 0.08
6.214	i'	T193/MISTRAL	20.09 ± 0.11
6.242	z'	T193/MISTRAL	19.46 ± 0.14
8.235	r'	T120	21.37 ± 0.10
9.220	i'	T193/MISTRAL	20.83 ± 0.11
9.262	z'	T193/MISTRAL	19.96 ± 0.13

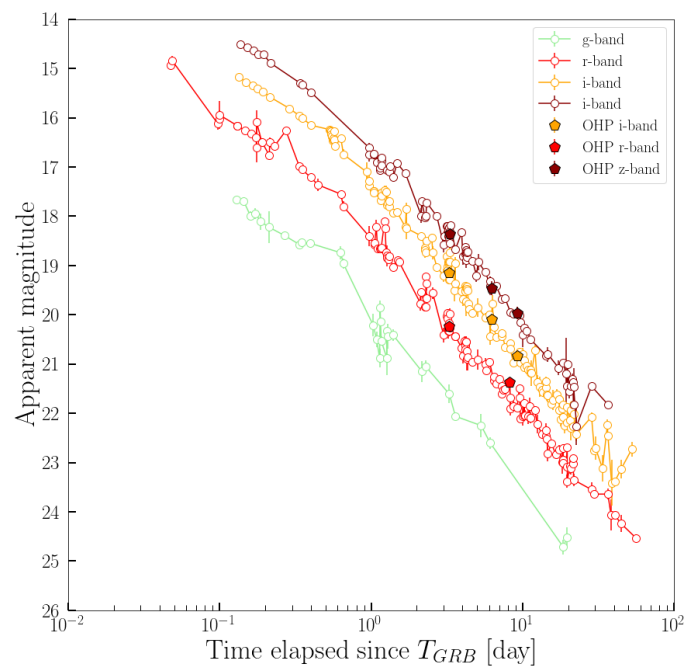


Fig. 13. The optical and NIR afterglow lightcurve of GRB 221009A. The OHP observations (T193/MISTRAL and T120) are shown as colored pentagons. The literature data are collected from (Fulton et al. 2023; Laskar et al. 2023).

5. Conclusions

The spectro-imager MISTRAL is installed at the folded Cassegrain focus of the 1.93m telescope at Haute-Provence Observatory since 2021 and running smoothly. It covers the spectral range from 4000 \AA to 10000 \AA in two settings, blue or red, at an average spectral resolution of 700. At the moment, two gratings, and five broad-band filters (g' , r' , i' , z' , Y) are available, plus some narrow-band filters around the main emission lines. Room is available for more gratings and filters to be installed in the future. The total throughput has been measured around 22% at the peak efficiency of 6000 \AA , with the present deep-depletion CCD of 2048 pixels of 13.5 microns each. The efficiency is dropping rapidly below 4000 \AA due to the poor transmission of the actual "blue" camera objective, but this will be replaced by a custom-made new objective which will cover the full spectral range, avoiding time-consuming changeovers. A limiting magnitude of $r \sim 19$ can be obtained in one hour of spectroscopy, while limiting magnitudes in the range of 20-21 are achieved in imaging mode

in 10–20mn exposures, depending on the exact filter and local seeing conditions. A specific interface is available, showing the nature and position of all optical elements, making the instrument very users friendly. It can be put into operations in less than 15mn (change-over from the other, permanently mounted instrument, Sophie), as required by the scientific program. On-sky tests with various types of objects have shown the operability and versatility of Mistral: we give a few examples of emission-line stars, novae, young stellar objects or galaxies, with particular emphasis on the follow-up of GRB's, which are likely to become a major source of targets with the launch of the SVOM satellite in 2024.

Acknowledgements. Authors acknowledge the efficient support of the OHP night operators, in particular J. Balcaen, Y. Degot-Longhi, S. Favard, and J.P. Troncin. Based on observations made at Observatoire de Haute Provence (CNRS), France, with MISTRAL on the T193 telescope, with AURELIE on the T152 telescope and with the CCD camera of the T120 telescope. We warmly thank Marco Lam for his contribution to the MISTRAL spectroscopic reduction software. We also acknowledge very useful discussions, during the conception phase, with the SPRAT team, in particular Iain Steele and Andrzej Piascik. This research has made use of the MISTRAL database, operated at CeSAM (LAM), Marseille, France. This work received support from the French government under the France2030 investment plan, as part of the initiative d'Excellence d'Aix-Marseille Université- A*MIDEX (AMX-19-IET-008). We were also supported by the IPhU Graduate School program at Aix-Marseille University. EJ is a FNRS Senior Research Associate. TRAPPIST is a project funded by the Belgian Fonds (National) de la Recherche Scientifique (F.R.S.-FNRS) under grant T.0120.21. We also acknowledge the support by Master Erasmus Mundus Europhotomics (599098-EPP-1-2018-1-FR-EPPKA1-JMD-MOB) financed by EACEA (European Education and Culture Executive Agency). Authors thank the CNES for financial support of the MISTRAL operations. Authors thank the former Pythéas institute director, N. Thouveny, for his great contribution to the MISTRAL instrument. Authors thanks T. Adami and J. Hornstein for their contributions to the GRB alert system and the data reduction tools. Authors thank A. DelSanti for useful discussions for the C/2022 E3 (ZTF) comet observations.

References

- Adami, C., Adami, T., Schneider, B., et al. 2023a, GRB Coordinates Network, 34418, 1
- Adami, C., Amram, P., Basa, S., et al. 2023b, GRB Coordinates Network, 34743, 1
- Adami, C., Basa, S., Le Floch, E., et al. 2023c, GRB Coordinates Network, 33741, 1
- Adami, C., Cuillandre, J. C., Ollivier, M., et al. 2023d, GRB Coordinates Network, 34247, 1
- Adami, C., Garnichey, M., Michel, F., et al. 2023e, GRB Coordinates Network, 33707, 1
- Adami, C., Grosso, N., Dennefeld, M., et al. 2021, The Astronomer Telegram, 15131
- Adami, C., Le Floch, E., Götz, D., et al. 2023f, GRB Coordinates Network, 35286, 1
- Adami, C., Palmerio, J., Vergani, S. D., et al. 2023g, GRB Coordinates Network, 33749, 1
- Adami, C., Schneider, B., Basa, S., et al. 2023h, GRB Coordinates Network, 33607, 1
- Adami, C., Schneider, B., Birlan, M., et al. 2023i, GRB Coordinates Network, 33537, 1
- Adami, T., Adami, C., Turpin, D., et al. 2023j, GRB Coordinates Network, 34030, 1
- Aharonian, F., Ait Benkhali, F., Aschersleben, J., et al. 2023, ApJ, 946, L27
- A'Hearn, M. F., Schleicher, D. G., Millis, R. L., Feldman, P. D., & Thompson, D. T. 1984, AJ, 89, 579
- Amram, P., Adami, C., Basa, S., et al. 2023, GRB Coordinates Network, 34762, 1
- An, Z.-H., Antier, S., Bi, X.-Z., et al. 2023, arXiv e-prints, arXiv:2303.01203
- Andrillat, Y., Baranne, A., & Houziaux, L. 1975, A&A, 41, 99
- Aravind, K., Ganesh, S., Venkataramani, K., et al. 2021, MNRAS, 502, 3491
- Aravind, K., Halder, P., Ganesh, S., et al. 2022, Icarus, 383, 115042
- Basa, S., Adami, C., Degot-Longhi, Y., et al. 2023, GRB Coordinates Network, 35384, 1
- Becker, A. 2015, HOTPANTS: High Order Transform of PSF ANd Template Subtraction
- Bertin, E. & Arnouts, S. 1996, A&AS, 117, 393
- Boch, T., Fernique, P., Bonnarel, F., et al. 2020, in Astronomical Society of the Pacific Conference Series, Vol. 527, Astronomical Society of the Pacific Conference Series, ed. R. Pizzo, E. R. Deul, J. D. Mol, J. de Plaa, & H. Verkouter, 121
- Bohlin, R. C., Gordon, K. D., & Tremblay, P. E. 2014, PASP, 126, 711
- Bradley, L., Sipőcz, B., Robitaille, T., et al. 2021, astropy/photutils: 1.1.0
- Burns, E., Svinikin, D., Fenimore, E., et al. 2023, ApJ, 946, L31
- Cao, Z., Aharonian, F., An, Q., et al. 2023, Science Advances, 9, eadj2778
- Chambers, K. C., Magnier, E. A., Metcalfe, N., et al. 2016, arXiv e-prints, arXiv:1612.05560
- Chavarría, C., de Lara, E., Finkenzeller, U., Appenzeller, I., & Cardona, O. 1983, A&A, 118, 189
- Courtès, G. 1960, Annales d'Astrophysique, 23, 115
- Dai, C.-Y., Wang, X.-Y., Liu, R.-Y., & Zhang, B. 2023, ApJ, 957, L32
- Danks, A. C. & Dennefeld, M. 1994, PASP, 106, 382
- Drilling, J. S., Jeffery, C. S., Heber, U., Moehler, S., & Napiwotzki, R. 2013, A&A, 551, A31
- Farnham, T. L., Schleicher, D. G., & A'Hearn, M. F. 2000, Icarus, 147, 180
- Feige, J. 1958, ApJ, 128, 267
- Finke, J. D. & Razzaque, S. 2023, ApJ, 942, L21
- Fulton, M. D., Smartt, S. J., Rhodes, L., et al. 2023, ApJ, 946, L22
- Gal-Yam, A. 2017, in Handbook of Supernovae, ed. A. W. Alsabti & P. Murdin, 195
- Gehrels, N., Chincarini, G., Giommi, P., et al. 2004, ApJ, 611, 1005
- Gehrels, N., Ramirez-Ruiz, E., & Fox, D. B. 2009, ARA&A, 47, 567
- Gill, R. & Granot, J. 2023, MNRAS, 524, L78
- Gillet, D., Burnage, R., Kohler, D., et al. 1994, A&AS, 108, 181
- Graham, M. J., Kulkarni, S. R., Bellm, E. C., et al. 2019, PASP, 131, 078001
- Hartigan, P., Edwards, S., & Ghandour, L. 1995, ApJ, 452, 736
- Haser, L. 1957, Bulletin de la Societe Royale des Sciences de Liege, 43, 740
- Herbig, G. H. & Bell, K. R. 1988, Third Catalog of Emission-Line Stars of the Orion Population : 3 : 1988, ed. K. R. Herbig, G. H. & Bell
- Herbig, G. H. & Dahm, S. E. 2006, AJ, 131, 1530
- Herbig, G. H. & Rao, N. K. 1972, ApJ, 174, 401
- Hodgkin, S. T., Breedt, E., Delgado, A., et al. 2021, Transient Name Server Discovery Report, 2021-4073, 1
- Hussenot-Desenonges, T., Wouters, T., Guessoum, N., et al. 2023, arXiv e-prints, arXiv:2310.14310
- Jayasinghe, T., Dixon, D., Povich, M. S., et al. 2019, MNRAS, 488, 1141
- Jehin, E., Vander Donckt, M., Manfroid, J., et al. 2022, The Astronomer's Telegram, 15822, 1
- Kann, D. A., Agayeva, S., Aivazyan, V., et al. 2023, ApJ, 948, L12
- Karpov, S. 2021, STDPipe: Simple Transient Detection Pipeline
- Koulouridis, E., Clerc, N., Sadibekova, T., et al. 2021, A&A, 652, A12
- Lam, M. C., Smith, R. J., Arcavi, I., et al. 2023, AJ, 166, 13
- Laskar, T., Alexander, K. D., Margutti, R., et al. 2023, ApJ, 946, L23
- Lemaître, G., Kohler, D., Lacroix, D., Meunier, J. P., & Vin, A. 1990, A&A, 228, 546
- Lesage, S., Veres, P., Briggs, M. S., et al. 2023, ApJ, 952, L42
- Levan, A. J., Lamb, G. P., Schneider, B., et al. 2023, ApJ, 946, L28
- Lu, K.-X., Zhang, Z.-X., Huang, Y.-K., et al. 2021, Research in Astronomy and Astrophysics, 21, 183
- MacLeod, C. L., Ross, N. P., Lawrence, A., et al. 2016, MNRAS, 457, 389
- Malesani, D. B., Levan, A. J., Izzo, L., et al. 2023, arXiv e-prints, arXiv:2302.07891
- Mohanty, S., Jayawardhana, R., & Basri, G. 2005, ApJ, 626, 498
- Muzerolle, J., Calvet, N., & Hartmann, L. 2001, ApJ, 550, 944
- O'Connor, B., Troja, E., Ryan, G., et al. 2023, Science Advances, 9, eadi1405
- Oke, J. B. & Gunn, J. E. 1983, ApJ, 266, 713
- Parra-Ramos, K., Schneider, B., Adami, C., et al. 2023, GRB Coordinates Network, 34744, 1
- Piascik, A. S. 2017, PhD thesis, Liverpool John Moores University, UK
- Piran, T. & Ofengeim, D. D. 2023, arXiv e-prints, arXiv:2308.03031
- Reipurth, B., Pedrosa, A., & Lago, M. T. V. T. 1996, A&AS, 120, 229
- Ren, J., Wang, Y., & Dai, Z.-G. 2023, arXiv e-prints, arXiv:2310.15886
- Robertson, J. G. 2013, PASA, 30, e048
- Sargent, W. L. W. & Searle, L. 1968, ApJ, 152, 443
- Schneider, B., Adami, C., Le Floch, E., et al. 2022a, GRB Coordinates Network, 32753, 1
- Schneider, B., Adami, C., Palmerio, J. T., et al. 2023a, GRB Coordinates Network, 33790, 1
- Schneider, B., Le Floch, E., Adami, C., et al. 2023b, in SF2A-2023: Proceedings of the Annual meeting of the French Society of Astronomy and Astrophysics, ed. M. N'Diaye, A. Siebert, N. Lagarde, O. Venot, K. Baillière, M. Béthermin, E. Lagarde, J. Malzac, & J. Richard, 503–506
- Schneider, B., Turpin, D., Le Floch, E., et al. 2022b, GRB Coordinates Network, 32271, 1
- Stone, R. P. S. 1974a, ApJ, 193, 135
- Stone, R. P. S. 1974b, ApJ, 193, 135
- Stone, R. P. S. 1977, ApJ, 218, 767

- Turpin, D., Adami, C., Le Floch, E., et al. 2023a, GRB Coordinates Network, 33282, 1
- Turpin, D., Adami, C., Le Floch, E., et al. 2023b, GRB Coordinates Network, 35367, 1
- Turpin, D., Adami, C., Schneider, B., et al. 2023c, GRB Coordinates Network, 33696, 1
- Turpin, D., Adami, C., Schneider, B., Le Floch, E., & Basa, S. 2022, GRB Coordinates Network, 32360, 1
- Turpin, D., Adami, C., Schneider, B., et al. 2023d, GRB Coordinates Network, 34356, 1
- Vail, J. L., Li, M. L., Wise, J., et al. 2023, GRB Coordinates Network, 34730, 1
- van Dokkum, P. G. 2001, PASP, 113, 1420
- Vardanyan, V., Takhistov, V., Ata, M., & Murase, K. 2022, arXiv e-prints, arXiv:2212.02436
- Veres, P., Burns, E., Bissaldi, E., et al. 2022, GRB Coordinates Network, 32636, 1
- Wei, J., Cordier, B., Antier, S., et al. 2016, arXiv e-prints, arXiv:1610.06892
- White, R. J. & Basri, G. 2003, ApJ, 582, 1109
- Williams, M. A., Kennea, J. A., Dichiara, S., et al. 2023, ApJ, 946, L24
- Yamashita, M., Itoh, Y., & Takagi, Y. 2020, PASJ, 72, 80
- Yang, Y.-M., Bi, X.-J., & Yin, P.-F. 2023, arXiv e-prints, arXiv:2312.09079
- Zhang, B., Wang, X.-Y., & Zheng, J.-H. 2023, arXiv e-prints, arXiv:2311.14180
- Zheng, J.-H., Wang, X.-Y., Liu, R.-Y., & Zhang, B. 2023, arXiv e-prints, arXiv:2310.12856

Appendix A: Exposure Time Calculators

We describe below the various parameters needed for the Exposure Time Calculators to operate, and how we obtained the results presented. ETC1 is for spectroscopy, and ETC 2 for imaging. We note that ETCs will be updated when the single lens described in Section 2.6 will be installed on the instrument.

Appendix A.1: Spectroscopy

ETC1 requires to enter several parameters: the choice of grating (blue/red), the expected seeing, the target's V band magnitude, the required S/N for the expected most intense spectral line, the nature of this line (absorption or emission), and the physical shape of the target (point source or extended source modelled by a Gaussian). ETC1 is basically using a N-parameter space of these parameters and fits a model at the place of the target in the considered space in order to give an exposure time.

ETC1 requests also : (1) the Moon conditions in terms of Moon illumination (choice between 0.25, 0.5, 0.75 and 1) and object angular distance to the Moon (choice between 45°, 90°, 135° and 180°), (2) the extended (or not) nature of the object (3) if needed, the intrinsic FWHM of the object if modeled by a Gaussian. This is the angular size of the object before seeing convolution. At this step, ETC1 is computing the percentage of flux arriving on the CCD after convolution of the object's signal by the seeing and the slit (1.9arcsec wide at the moment). This percentage will be applied to the given target magnitude. (4) The Air Mass (using the OHP extinction curve). One can also add an additional extinction in magnitude to take into account a potential cloud-induced extinction.

ETC1 is now able to fit a model to real observations within the adapted space in order to give an estimated exposure time. 3D views similar to those on Fig.A.1 are also provided to allow the observer to manually adjust her/his exposure time estimate as a function of the location of the target in the 3D sheet (see Fig.A.1).

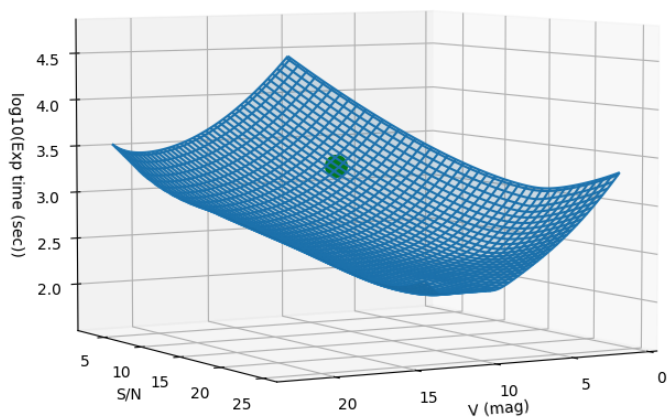


Fig. A.1. Example of ETC 3D sheet within the (magnitude, S/N, exposure time) space for the blue setting.

Appendix A.2: Imaging

Another exposure time calculator (ETC2) is available to give to the observer a typical exposure time for his/her targets in imaging mode. ETC2 gives the exposure time needed to detect objects at a given magnitude with the requested S/N.

These estimates are based on observations of several fields (XCLASS3091 cluster of galaxies, Koulouridis et al. (2021), Abell400 cluster of galaxies, and at2021ft transient field) observed in g', r', i', z' and Y bands under different seeing and airmasses. They were observed with different exposure times, between 1 min and 60 minutes. They were all at relatively low galactic latitudes, providing catalogs of several hundreds of stars. These stars were separated from galaxies using the SDSS images available for these fields. We used simulations to degrade the shape of these stars before re-detecting them (to take into account the seeing and object extension). ETC2 is then using a N-parameter space of these characteristics and fit a polynomial function (order 2) for the place of the target in order to give an exposure time.

Similarly to ETC1, the technique used to generate an exposure time typically consists in the following steps: (1) select the filter you want to use in imaging. (2) give the expected seeing. (3) give the extended (or not) nature of the object (4) if needed, give the intrinsic FWHM of the object if modeled by a Gaussian; this is the angular size of the object before seeing convolution. (5) give an additional extinction in magnitudes to take into account a potential cloud-induced extinction. (6) give the Air Mass to compute the magnitude loss due to the atmosphere (using the OHP extinction curve). (7) give the target's magnitude. (8) give the required S/N.

ETC2 is now able to fit a polynomial model on real observations within the chosen space in order to give an estimated exposure time. 3D views similar to those on Fig.A.1 are also provided to allow the observer to manually adjust exposure time estimate as a function of the location of the target in the explored space. ETC2 will give the exposure time needed to detect objects at the required magnitude to have S/N larger than the required one.

Appendix B: Filter Responses

Filter responses²⁰ are summarized in Table B.1 and shown in Fig.B.1.

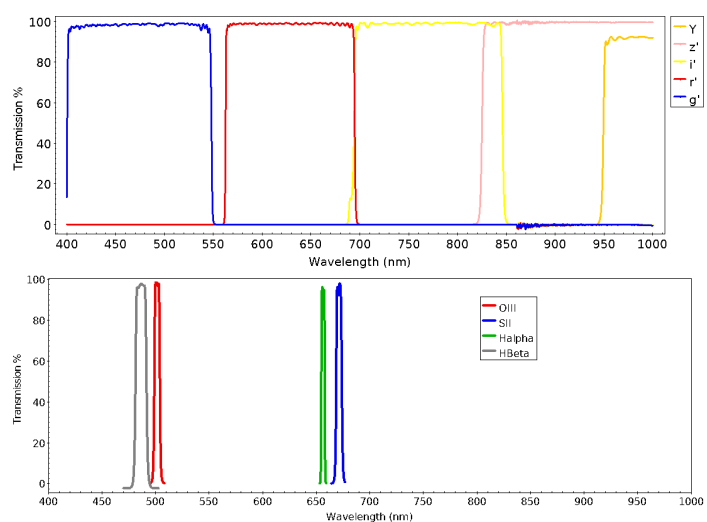


Fig. B.1. Profiles of the g', r', i', z', Y, H β , OIII, H α , and SII filters described in Table B.1.

The MISTRAL filters transmission was measured with the Laboratoire d'Astrophysique de Marseille Perkin-Elmer spec-

²⁰ see http://www.obs-hp.fr/guide/mistral/filter_characteristics.html

trograph between 4000 and 10000 Å, using the PMT and InGaAs sources and low (4 Å) and high (2 Å) resolution. The wide range filters (g', r', i', z', Y, passe-haut 4000-10000 Å, passe-haut 6000-10000 Å) were measured with a resolution of 4 Å (one measured point every 2 Å with a measured width of 4 Å). The narrow-band filters (Hβ, OIII, Hα, SII) were measured with same set-up between 4000 and 10000 Å and with a better resolution of 2 Å (one measured point every Å with a measured width of 2 Å) around their useful domain.

The accuracy of the measurements was evaluated by comparing the results between two consecutive measures (without filter repositioning between two measures) and was estimated with the SII filter measured at high resolution. The difference between two consecutive measures is well below the 1% level, and the shift in wavelength is lower than 0.1 Å.

Appendix C: MISTRAL spectral resolving-power estimates

The spectral resolving-power, $R \equiv \lambda/\text{FWHM}$ with FWHM the full-width at half maximum of the sharp line (Robertson 2013), was computed for the blue and red configurations of MISTRAL (Table C.1). The linear fitting of these data (Fig. C.1) provides the following formulae of R vs. the wavelength for the blue and red configurations, normalised at the wavelength of the Hα line:

$$R^{\text{Blue}}\left(\frac{\lambda}{\text{Å}}\right) = 781.4 + 675.7 \left(\frac{\lambda}{6562.83 \text{ Å}} - 1 \right) \quad (\text{C.1})$$

$$R^{\text{Red}}\left(\frac{\lambda}{\text{Å}}\right) = 832.4 + 541.4 \left(\frac{\lambda}{6562.83 \text{ Å}} - 1 \right) \quad (\text{C.2})$$

Therefore, the spectral resolving-power at the Hα line is ~7% better in the red configuration.

From high-resolution ($R \sim 33,000$) optical spectra of T Tauri stars and brown dwarfs, it was demonstrated empirically that the full width at 10% of the Hα emission profile peak (hereafter FW10%Hα) can be used as an indicator of accretion when it is larger than 270 km s⁻¹ (White & Basri 2003). To use this criteria with MISTRAL spectrum, the observed Hα FWHM must be first corrected of the MISTRAL (Gaussian) line-spread function to estimate the intrinsic FWHM of Hα: $\text{FWHM}_{\text{int}}^2 = \text{FWHM}_{\text{obs}}^2 - \text{FWHM}_{\text{MISTRAL}}^2$. Then, using $\text{FW10\%H}\alpha = \sqrt{\ln(10)/\ln(2)} \text{FWHM}$, we derive the velocity width corresponding to FW10%Hα vs. the observed Hα FWHM:

$$\frac{v}{\text{km s}^{-1}} = \sqrt{\frac{\ln(10)}{\ln(2)}} \times \frac{c}{R(H\alpha)} \times \sqrt{\left(R(H\alpha) \frac{\text{FWHM}_{\text{obs}}}{6562.83} \right)^2 - 1}, \quad (\text{C.3})$$

with c , the speed of light.

Appendix D: Spectrograph sensitivity and telluric corrections using Feige 15 in the red configuration of MISTRAL

The spectrophotometric standard Feige 15 is a faint, blue star of the galactic halo (Feige 1958). The determination of its spectral type has evolved from A1 V (Sargent & Searle 1968) to

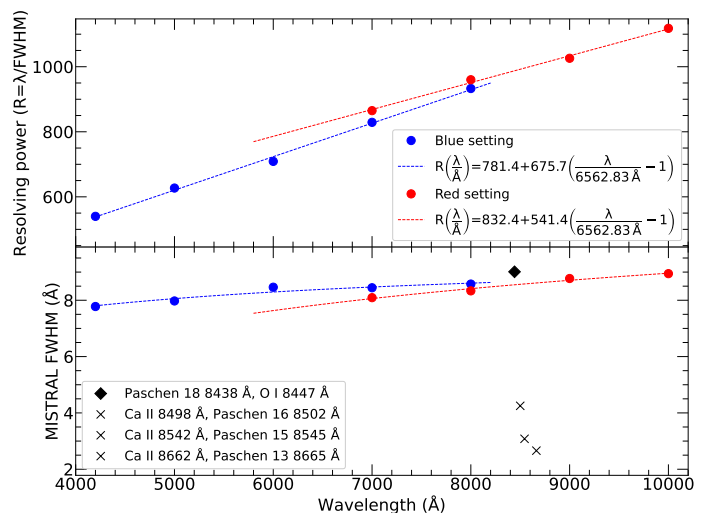


Fig. C.1. Theoretical spectral resolving-power of MISTRAL. The data for the blue and red configurations are from Table C.1. *Top panel:* resolving power vs. wavelength. The straight lines are the linear fitting of these data. *Bottom panel:* FWHM vs. wavelength. The curves are computed from the linear fits. For comparison, the wavelength separation of several close stellar emission lines are marked with diamond and crosses if resolved or not, respectively, with MISTRAL.

sdA0IV:He1 (Drilling et al. 2013). Its spectral energy distribution (SED) is only reported from 3200 to 8370 Å (Stone 1977), using band widths of 49 Å and 98 Å in the wavelength ranges 3200–5263 and 5263–8370 Å, respectively (Stone 1974b). Therefore, Feige 15 is routinely used for the spectral calibration of MISTRAL in the blue configuration; but, its SED must be extended above 8370 Å to be used in the red configuration.

We have adapted the `get_sensitivity` function of ASPIRED²¹ (Lam et al. 2023) to use the bandwidths of the reference fluxes when determining the spectrograph sensitivity from the standard spectrum. We have written a custom python script to use the CALSPEC²² spectrum of α Lyrae (Vega), normalised on the band width centered at 8370 Å, to extend the SED longwards. We compute the fluxes of this A0 template within bandwidths of 25, 100, and 100 Å centered at 8807 (mean of the Pa 11 and Pa 12 wavelengths), 9740, and 9850 Å, respectively, outside the atmospheric absorption band of water (Lu et al. 2021), which leads to 10.679, 10.780, and 10.800 ABmag, respectively.

Fig. D.1 shows the reduced spectrum of Feige 15 as observed at airmass 1.16, where the standard fluxes match the literature fluxes (Stone 1977) plus these three new references of flux. The observed depths of the Paschen lines have a very good match outside the atmospheric absorption band of water with the A0 template, which can hence also be used for telluric correction in this atmospheric absorption band.

We estimate the standard continuum shortwards of 8370 Å after excluding the atmospheric absorption bands. The ratio inside the atmospheric absorption bands between the standard con-

²¹ http://www.obs-hp.fr/guide/mistral/MISTRAL_spectrograph_camera.shtml#H5

²² <https://www.stsci.edu/hst/instrumentation/reference-data-for-calibration-and-tools/astronomical-catalogs/calspechttps://www.stsci.edu/hst/instrumentation/reference-data-for-calibration-and-tools/astronomical-catalogs/calspec>

Table B.1. MISTRAL filters response functions.

Name	Central λ	Maximum Transmission	50% low	50% high
SDSS g'	$\sim 4700 \text{ \AA}$	$\geq 99\%$	4010 \AA	5490 \AA
SDSS r'	$\sim 6300 \text{ \AA}$	$\geq 99\%$	5630 \AA	6950 \AA
SDSS i'	$\sim 7700 \text{ \AA}$	$\geq 99\%$	6940 \AA	8470 \AA
SDSS z'	$\sim 8400 \text{ \AA}$	$\geq 99\%$	8250 \AA	
Y	$\geq 9500 \text{ \AA}$	$\geq 92\%$	9500 \AA	
H β	$\sim 4860 \text{ \AA}$	$\geq 92\%$	4810 \AA	4920 \AA
OIII	$\sim 5020 \text{ \AA}$	$\geq 98\%$	4990 \AA	5041 \AA
H α	$\sim 6565 \text{ \AA}$	$\geq 96\%$	6548 \AA	6580 \AA
SII	$\sim 6710 \text{ \AA}$	$\geq 97\%$	6687 \AA	6740 \AA
Long Pass OD4 4000 \AA	$\geq 4000 \text{ \AA}$	$\geq 98\%$	4000 \AA	
Long Pass OD4 6000 \AA	$\geq 6000 \text{ \AA}$	$\geq 98\%$	5994 \AA	
Long Pass smooth 4000 \AA	$\geq 4000 \text{ \AA}$	$\geq 90\%$	4000 \AA	
Long Pass smooth 6000 \AA	$\geq 6000 \text{ \AA}$	$\geq 90\%$	5706 \AA	

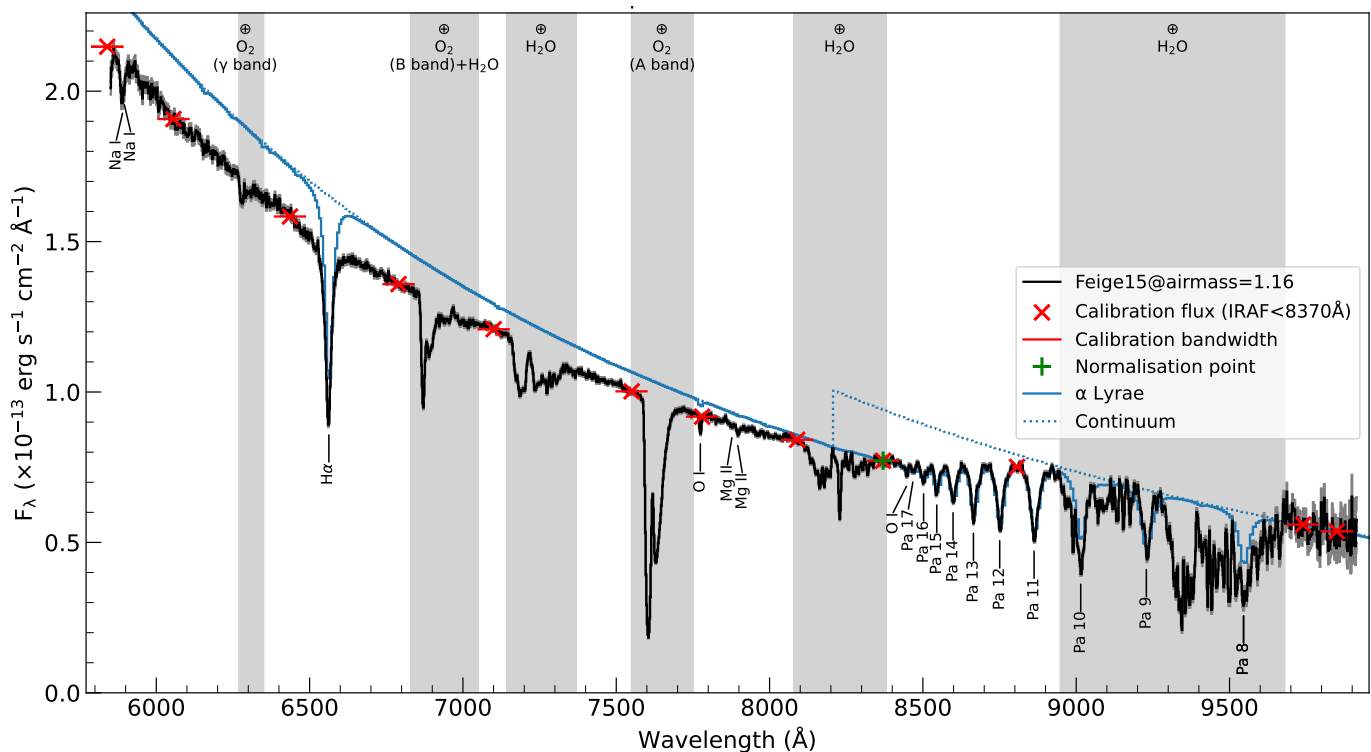


Fig. D.1. MISTRAL red configuration spectrum of the spectrophotometric standard Feige 15, obtained with an exposure of 600 s on the night of 2021 Dec. 8 (no telluric correction). The flux error-bars are plotted in gray. The vertical light-gray stripes indicate the atmospheric absorption bands of water and molecular oxygen (Lu et al. 2021). The reference flux and bandwidth wavelengths are marked in red (Stone 1977, shortwards of 8370 \AA). The solid and dotted blue lines are the α Lyrae (Vega) CALSPEC spectrum and continuum (Bohlin et al. 2014), respectively, normalised at the wavelength and flux marked by the green plus.

tinuum (shortwards of 8370 \AA) or the A0 template (longwards of 8370 \AA) and the observed flux is used for the telluric correction of the spectrum of LkH α 324SE (Fig. 6).

Appendix E: CCD reading modes

Several CCD reading modes are available (nominal temperature of the CCD: $\sim 90\text{C}$, saturation level: $\sim 60\,000$). Two modes have been extensively tested and they are the only ones offered: fast mode (3 MHz) and slow mode (50 kHz). They are briefly described in Table E.1. The fast mode is adapted for technical operations such as telescope focus or pointing, thanks to the very

short reading time allowing e.g. real-time object focusing. For science operations, a slow mode is offered with a nearly three times lower read-out noise.

Appendix F: Instrument stability

One of the science goals of MISTRAL being the long-time follow-ups of variable objects, it is important to evaluate its stability over time.

We therefore investigated the CCD mean electronic noise level with the 760 measured bias frames over an operating period of ~ 3 years. Fig. F.1 shows the variation of the mean ADU

Table C.1. MISTRAL theoretical spectral resolving-power.

Wavelength (Å)	R
Blue configuration	
4200	540
5000	627
6000	709
7000	829
8000	933
Red configuration	
7000	865
8000	960
9000	1026
10000	1118

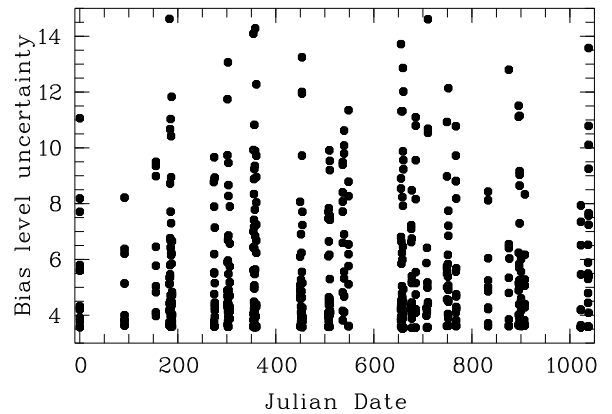
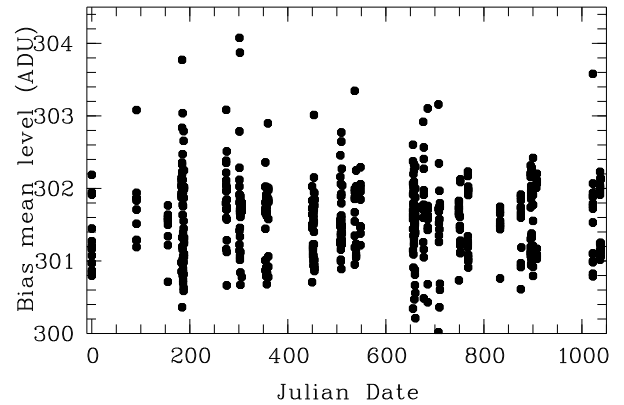
Table E.1. Characteristics of the different reading modes.

	Fast mode: 3 MHz	Slow mode: 50 kHz
Read Out Noise	11 e-	4 e-
Reading time	0.7 sec	40 sec
Gain in e-/ADU	1.03	1.03

level and of the $1\text{-}\sigma$ mean level uncertainty of biases over a period of 1050 days. Both are compatible with no variation over time, with a bias level of 302 ± 6 ADUs.

We then investigated the response of the CCD when illuminated by an artificial source (to avoid sky variability and telescope primary mirror coating variations). We used for this the 917 available arc calibration frames, selecting only the 30sec exposures made with the blue dispersor. Fig. F.2 shows the variation of the mean flux level of these exposures (upper panel). After an initial 15%-decrease of the flux during the first year probably due to the wavelength calibration lamp aging, the mean flux is remaining constant since almost two years.

We finally estimated the variation of the percentage of low-response CCD pixels. For each arc frames, we computed the number of pixels with an ADU level below 320. This corresponds to the mean bias level plus 3σ . Every pixel below this level may be a low-response pixel because still compatible with a bias level despite the 30sec exposure with the calibration lamps "on". Fig. F.2 shows a very low and stable level of these pixels, around 0.2% of the total number of CCD pixels.

**Fig. F.1.** Variation over time (starting at the Julian Date of 2459310) of the mean ADU level (top panel) and of the $1\text{-}\sigma$ mean level uncertainty (bottom panel) of MISTRAL's biases.

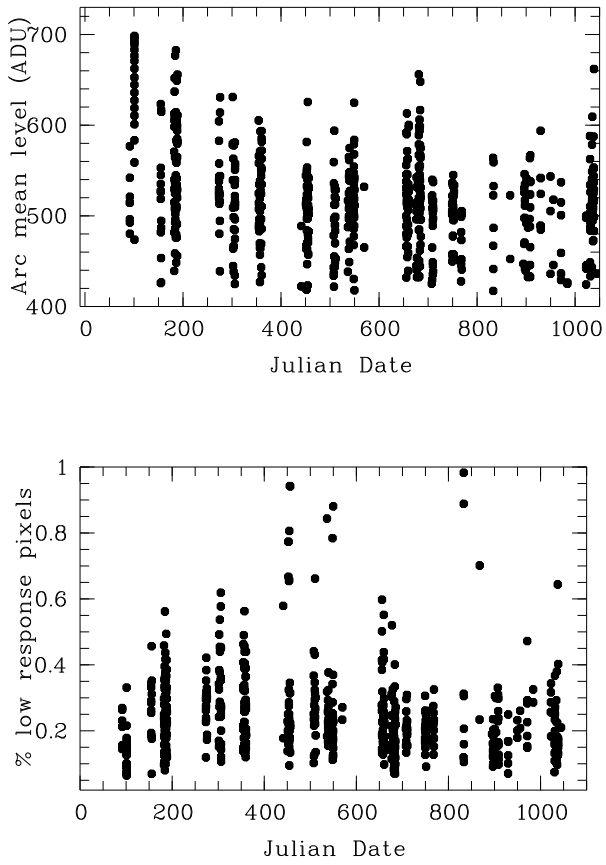


Fig. F.2. Variation over time (starting at the Julian Date of 2459310) of the mean ADU level (top panel) of MISTRAL's arc exposures. Bottom panel shows the percentage of potential low-response pixels over time.